The Astronomical Journal, 165:121 (17pp), 2023 March https://doi.org/10.3847/1538-3881/acb5a2

TOI-4562b: A Highly Eccentric Temperate Jupiter Analog Orbiting a Young Field Star

Alexis Heitzmann[1,11], George Zhou[1], Samuel N. Quinn[2], Chelsea X. Huang[1], Jiayin Dong[3,4,5,37], L. G. Bouma[6,38], Rebekah I. Dawson[4,5], Stephen C. Marsden[1], Duncan Wright[1], Pascal Petit[7], Karen A. Collins[2], Khalid Barkaoui[8,9,10], Robert A. Wittenmyer[1], Edward Gillen[11,12,39], Rafael Brahm[13,14], Melissa Hobson[14,15], Coel Hellier[16], Carl Ziegler[17], César Briceño[18], Nicholas Law[19], Andrew W. Mann[19], Steve B. Howell[20], Crystal L. Gnilka[20], Colin Littlefield[20,21], David W. Latham[2], Jack J. Lissauer[22], Elisabeth R. Newton[23], Daniel M. Krolikowski[24], Ronan Kerr[24], Rayna Rampalli[23], Stephanie T. Douglas[25], Nora L. Eisner[26], Nathalie Guedj[27], Guoyou Sun[27], Martin Smit[27], Marc Huten[27], Thorsten Eschweiler[27], Lyu Abe[28], Tristan Guillot[28], George Ricker[29], Roland Vanderspek[29], Sara Seager[29,30,31], Jon M. Jenkins[20], Eric B. Ting[20], Joshua N. Winn[32], David R. Ciardi[33], Andrew M. Vanderburg[29,34], Christopher J. Burke[29], David R. Rodriguez[35], and Tansu Daylan[32,36]

[1] University of Southern Queensland, Centre for Astrophysics, West Street, Toowoomba, QLD 4350, Australia; alexis.heitzmann@usq.edu.au
[2] Center for Astrophysics | Harvard & Smithsonian, 60 Garden Street, Cambridge, MA 02138, USA
[3] Center for Computational Astrophysics, Flatiron Institute, 162 Fifth Avenue, New York, NY 10010, USA
[4] Department of Astronomy & Astrophysics, 525 Davey Laboratory, The Pennsylvania State University, University Park, PA 16802, USA
[5] Center for Exoplanets and Habitable Worlds, 525 Davey Laboratory, The Pennsylvania State University, University Park, PA 16802, USA
[6] Cahill Center for Astrophysics, California Institute of Technology, Pasadena, CA 91125, USA
[7] Institut de Recherche en Astrophysique et Planétologie, Université de Toulouse, CNRS, CNES, 14 avenue Edouard Belin, F-31400 Toulouse, France
[8] Astrobiology Research Unit, Université de Liège, 19C Allée du 6 Août, B-4000 Liège, Belgium
[9] Department of Earth, Atmospheric and Planetary Science, Massachusetts Institute of Technology, 77 Massachusetts Avenue, Cambridge, MA 02139, USA
[10] Instituto de Astrofísica de Canarias (IAC), Calle Vía Láctea s/n, E-38200, La Laguna, Tenerife, Spain
[11] Astronomy Unit, Queen Mary University of London, Mile End Road, London E1 4NS, UK
[12] Astrophysics Group, Cavendish Laboratory, J.J. Thomson Avenue, Cambridge CB3 0HE, UK
[13] Facultad de Ingeniería y Ciencias, Universidad Adolfo Ibáñez, Av. Diagonal las Torres 2640, Peñalolén, Santiago, Chile
[14] Millennium Institute of Astrophysics MAS, Nuncio Monsenor Sotero Sanz 100, Of. 104, Providencia, Santiago, Chile
[15] Max Planck Institute for Astronomy, Königstuhl 17, D-69117–Heidelberg, Germany
[16] Astrophysics Group, Keele University, Staffordshire, ST5 5BG, UK
[17] Department of Physics, Engineering and Astronomy, Stephen F. Austin State University, 1936 North Street, Nacogdoches, TX 75962, USA
[18] Cerro Tololo Inter-American Observatory, Casilla 603, La Serena, Chile
[19] Department of Physics and Astronomy, The University of North Carolina at Chapel Hill, Chapel Hill, NC 27599-3255, USA
[20] NASA Ames Research Center, Moffett Field, CA 94035, USA
[21] Bay Area Environmental Research Institute, Moffett Field, CA 94035, USA
[22] Space Science & Astrobiology Division , MS 245-3, NASA Ames Research Center, Moffett Field, CA 94035, USA
[23] Department of Physics and Astronomy, Dartmouth College, Hanover, NH 03755, USA
[24] Department of Astronomy, The University of Texas at Austin, Austin, TX 78712, USA
[25] Department of Physics, Lafayette College, 730 High Street, Easton, PA 18042, USA
[26] Sub-department of Astrophysics, University of Oxford, Keble Road, Oxford, UK
[27] Citizen Scientist, Zooniverse c/o University of Oxford, Keble Road, Oxford OX1 3RH, UK
[28] Université Côte d'Azur, Observatoire de la Côte d'Azur, CNRS, Laboratoire Lagrange, CS 34229, F-06304 Nice Cedex 4, France
[29] Department of Physics and Kavli Institute for Astrophysics and Space Research, Massachusetts Institute of Technology, Cambridge, MA 02139, USA
[30] Department of Earth, Atmospheric, and Planetary Sciences, Massachusetts Institute of Technology, Cambridge, MA 02139, USA
[31] Department of Aeronautics and Astronautics, Massachusetts Institute of Technology, Cambridge, MA 02139, USA
[32] Department of Astrophysical Sciences, Princeton University, Princeton, NJ 08544, USA
[33] NASA Exoplanet Science Institute, Caltech/IPAC, 1200 E. California Avenue, Pasadena, CA 91125, USA
[34] Department of Astronomy, University of Wisconsin-Madison, Madison, WI 53706, USA
[35] Space Telescope Science Institute, 3700 San Martin Drive, Baltimore, MD, 21218, USA
Received 2022 August 24; revised 2023 January 13; accepted 2023 January 20; published 2023 February 22

Abstract

We report the discovery of TOI-4562b (TIC-349576261), a Jovian planet orbiting a young F7V-type star, younger than the Praesepe/Hyades clusters (<700 Myr). This planet stands out because of its unusually long orbital period for transiting planets with known masses ($P_{\rm orb} = 225.11781^{+0.00025}_{-0.00022}$ days) and because it has a substantial eccentricity ($e = 0.76^{+0.02}_{-0.02}$). The location of TOI-4562 near the southern continuous viewing zone of TESS allowed observations throughout 25 sectors, enabling an unambiguous period measurement from TESS alone. Alongside the four available TESS transits, we performed follow-up photometry using the South African Astronomical Observatory node of the Las Cumbres Observatory and spectroscopy with the CHIRON spectrograph on the 1.5 m

[36] LSSTC Catalyst Fellow.
[37] Flatiron Research Fellow.
[38] 51 Pegasi b Fellow.
[39] Winton Fellow.

SMARTS telescope. We measure a radius of $1.118^{-0.014}_{+0.013}\,R_{\rm J}$ and a mass of $2.30^{+0.48}_{-0.47}\,M_{\rm J}$ for TOI-4562b. The radius of the planet is consistent with contraction models describing the early evolution of the size of giant planets. We detect tentative transit timing variations at the ∼20 minutes level from five transit events, favoring the presence of a companion that could explain the dynamical history of this system if confirmed by future follow-up observations. With its current orbital configuration, tidal timescales are too long for TOI-4562b to become a hot Jupiter via high-eccentricity migration though it is not excluded that interactions with the possible companion could modify TOI-4562b's eccentricity and trigger circularization. The characterization of more such young systems is essential to set constraints on models describing giant-planet evolution.

Unified Astronomy Thesaurus concepts: Exoplanets (498); Exoplanet migration (2205); Young stellar objects (1834); Extrasolar gaseous giant planets (509); Elliptical orbits (457); Stellar activity (1580); Transit timing variation method (1710)

1. Introduction

Planetary systems evolve rapidly within the first hundreds of millions of years of formation. The architectures of the systems evolve before settling into their eventual orbital configuration. Planets with extensive gaseous envelopes are expected to undergo contraction and cooling and experience observable changes in radius within this time frame. Observations of planets around young stars help anchor our understanding of this era of rapid change and help define models of planet formation and evolution. In particular, Jovian planets in distant orbits are less affected by stellar irradiation than close-in hot Jupiters. Transiting cold Jupiters around young stars can therefore provide constraints for cooling and contraction of giant-planet evolution models. The orbital properties of these planets can also help to narrow down the timescales of dynamical evolution experienced by many other giant planets discovered to date.

Numerous mechanisms are responsible for the formation and evolution of close-in Jovian planets. These mechanisms vary by the distribution of planets that they produce and by the timescales at which they operate. We can best assess the prevalence of these multiple formation channels via a census of the gas-giant population as a function of time (see Dawson & Johnson 2018). Such a temporal survey of planetary systems can unveil the roles that in situ formation (review in Chabrier et al. 2014), disk migration (review in Baruteau et al. 2014), and high-eccentricity migration (review in Dawson & Johnson 2018) played in shaping our current gas-giant population. For example, planets can gravitationally interact with their depleting gas disks, resulting in moderately eccentric final orbits within a few million years (e.g., Nagasawa et al. 2003; Duffell & Chiang 2015; Debras et al. 2021). On the other extreme, excitation via stellar flybys can occur on the hundreds-of-millions-of-years timescale (e.g., Shara et al. 2016).

Gas giants also undergo significant contraction in the first hundred million years after formation. In models, the rate of contraction is strongly dependent on the initial conditions of the planet after formation, such as their envelope-core mass ratio and initial luminosities (e.g., Fortney et al. 2007; Linder et al. 2019). It is clear, however, that the radius distribution of close-in Jovian planets is shaped by external factors that retard their contraction (e.g., Guillot & Showman 2002; Baraffe et al. 2003; Batygin & Stevenson 2010). Young planets in distant orbits provide simpler key tests for gas-giant evolution.

Missions like Kepler, K2, and the Transiting Exoplanet Survey Satellite (TESS; Ricker et al. 2015) have brought forth a growing number of planetary systems about young stars (e.g., Newton et al. 2019; Mann et al. 2020; Plavchan et al. 2020; Bouma et al. 2022a; Zhou et al. 2022). However, true young Jovian analogs are rare. Interestingly, Suárez Mascareño et al. (2022) measured the masses of the giant planets in the 22 Myr old V1298 Tau system (David et al. 2019a, 2019b), finding that the two Jovian planets have already settled to their expected final radii, a process that is predicted to take hundreds of millions of years by contraction models. Other close-in Jovian-sized planets have also been found around young stars (Bouma et al. 2020; Rizzuto et al. 2020; Mann et al. 2021), but strong stellar activity has yet prevented their mass from being measured.

We report the discovery of a young transiting Jovian planet in a distant orbit around a <700 Myr old star. TOI-4562 hosts a temperate Jupiter in a 225 day period orbit near the TESS continuous viewing zone. Along with additional observations from our ground-based photometric follow-up campaign, five total transits of the planet were obtained, unambiguously identifying the period of the system. Radial-velocity (RV) monitoring over the following 2 yr provided a mass and eccentricity measurement for the young planet. In addition, data from FEROS helped to constrain the stellar parameters, and high-resolution images from Gemini South and the Southern Astrophysical Research (SOAR) helped to rule out false positive scenarios, confirming the transit candidate as a true planet. We also constrained the age of TOI-4562 via gyrochronology and lithium. Finally, we detect a transit-timing variation (TTV) signature, indicative of a perturbing companion in the system. TOI-4562b is one of the longest-period transiting temperate Jupiters discovered by TESS and the youngest among such planets. Missions like TESS and PLATO (Rauer et al. 2014) have the potential to uncover this special population that critically constrains cooling models and migration pathways for Jovian planets.

2. Observations

2.1. TESS: Photometry

The transiting planet candidate around TOI-4562 was first identified from observations by TESS. TOI-4562 lies in the southern continuous viewing zone of TESS and therefore received near-uninterrupted photometric monitoring during years 1 and 3 of operations. The target received observations at 30 minute cadence during sectors 1–8 (2018 July 25 to 2019 February 28) and sectors 10–13 (2019 March 26 to 2019 July 18) and 2 minute target-pixel-stamp observations during sectors 27–39 (2020 July 4 to 2021 June 24). The transit signature of TOI-4562b was detected by the TESS Science Processing Operations Center (Jenkins et al. 2016) at NASA Ames Research Center during a transit search of sectors 27 through 39 with an adaptive, noise-compensating matched filter (Jenkins 2002; Jenkins et al. 2010, 2020). The transit signature passed all the diagnostic tests in the data validation report (Twicken et al. 2018) and was fitted with an initial limb-darkened transit model (Li et al. 2019). In particular, the transit signal passed the difference image centroiding test, which localized the source of the transits to within $1''.0 \pm 2''.5$. The TESS Science Office reviewed the diagnostic information and released an alert to the community for TOI-4562b on 2021 October 28 (Guerrero et al. 2021).

We make use of the MIT Quicklook pipeline (Huang et al. 2020) photometric extraction from the full-frame image observations. In addition, where available, we make use of the 2 minute cadence target-pixel-file observations from the crowding and flux fraction corrected Simple Aperture Photometry light curves (Twicken et al. 2010; Morris et al. 2020) made available by SPOC. Because of the large stellar variability seen in the light curve, we used the Simple Aperture Photometry (SAP) light curves rather than the Pre-search Data Conditioning SAP flux and performed the detrending using a high-order spline interpolation (Vanderburg & Johnson 2014)

The full TESS light curve covering all sectors of observations is presented in Figure 1. During the 2 (nonconsecutive) yr of near-continuous observations, a total of four transits were captured by TESS. Figure 2 shows the zoomed-in region around each of these transits.

TOI-4562 was first identified as a potential young star due to its strong rotational modulation (Zhou et al. 2021) as part of our program to survey for planets around young field stars. We performed a search for transiting signals around TOI-4562 via a box-least-squares period search (Kovacs et al. 2002) after removal of the stellar modulation signal with the splines. This detrending was not the one used for the transit modeling, described in Section 4.1.

2.2. Follow-up Photometry

We obtained follow-up photometric confirmation of the planetary transit via the Las Cumbres Observatory Global Network (LCOGT; Brown et al. 2013). Transit opportunities for a 225 day period planet are rare from the ground (see Table 3). We captured the full transit of TOI-4562b on 2022 January 3 UTC from the South African Astronomical Observatory (SAAO) node of LCOGT via two 1 m telescopes. The observations were obtained with the Sinistro 4 K × 4 K cameras in the Sloan i' filter. The observations were calibrated via the BANZAI pipeline (McCully et al. 2018), and light curves were extracted via the ASTROIMAGEJ package (Collins et al. 2017) using circular apertures with radius $4''.7$, which exclude flux from all known nearby Gaia EDR3 and TESS Input Catalog stars. The combined light curves (after removing systematics) and best-fit model are shown in Figure 2.

In addition, a transit on 2022 August 16 was attempted from the SAAO node of LCOGT via one 1 m telescope, as well as the Antarctica Search for Transiting ExoPlanets (ASTEP) facility (Guillot et al. 2015; Mekarnia et al. 2016), located at the East Antarctic plateau. A 25 minute segment was captured out of transit, but no portions of a transit event were recorded, and the data set is not included in the modeling presented below.

2.3. CHIRON/SMARTS: Spectroscopy

To characterize the radial-velocity orbit of TOI-4562b and constrain the properties of the host star, we obtained 84 spectroscopic observations of TOI-4562 using the CHIRON facility. To capture the long orbital period of TOI-4562b, the velocities spanned two observing seasons, from 2020 December 9 to 2022 January 23; the resulting radial velocities are given in Table 4. CHIRON is a fiber-fed, high-resolution echelle spectrograph on the 1.5 m SMARTS telescope at Cerro Tololo Inter-American Observatory, Chile (Tokovinin et al. 2013). Due to the faintness of the host star, spectral observations were obtained in the "fiber" mode of CHIRON, yielding a resolving power of $R \sim 28{,}000$ over the wavelength range of 4100–8700 Å and an average signal-to-noise of ∼100 per resolution element at the Mg b line wavelength region.

We make use of the extracted spectra from the standard CHIRON pipeline described in Paredes et al. (2021). Radial velocities were derived from the observations via a least-squares deconvolution against a nonrotating ATLAS9 spectral template (Castelli & Kurucz 2004). The resulting broadening profile is fitted via a kernel describing the effects of radial-velocity shift and rotational, macroturbulent, and instrumental broadening. The derived velocities are presented in Table 4 and shown in Figure 4.

To estimate the spectroscopic properties of the host star, we matched each spectrum against an observed library of ∼10,000 spectra preclassified by the spectroscopic classification pipeline (Buchhave et al. 2012). The matching was performed by first training the preclassified library via a gradient-boosting classifier using SCIKIT-LEARN and then classifying the observed spectrum. We found that TOI-4562 has an effective temperature of $T_{\rm eff} = 6096 \pm 50$ K, a surface gravity of $\log g = 4.4 \pm 0.1$ dex, a bulk metallicity of $[{\rm M/H}] = 0.1 \pm 0.1$ dex, and a line-of-sight projected stellar rotational velocity of $v \sin i = 17 \pm 0.5\ {\rm km\ s^{-1}}$. Since the CHIRON data set overwhelms the other data sets we obtained for TOI-4562 in quantity, we adopt these parameters as Gaussian priors in the global analysis of the system described in Section 4. We note a general consensus between the spectral parameters from CHIRON and those presented below in Section 2.4.

We also check for the possibility that the velocity variations we observe are due to a spectroscopically blended companion rather than the host star. We compare the broadening measured from the line profiles against the velocities and find no correlation. If a blended companion is causing the radial-velocity offset, then the line profiles should be broadest at the orbital quadratures and narrowest at the conjunctions. We therefore find no evidence that the velocity variations originate from a blended companion.

2.4. FEROS and GALAH: Spectroscopy

The FEROS spectrograph, attached to the MPG/ESO 2.2 m (Kaufer et al. 1999) telescope at La Silla Observatory, gathered 11 spectra of TOI-4562. Spectra are coadded with a signal-to-noise ratio per spectra ranging between 52 and 82, and atmospheric parameters are derived using ZASPE (Brahm et al. 2017b). We find $T_{\rm eff} = 6280 \pm 100$ K, $\log g = 4.49 \pm 0.10$, $[{\rm M/H}] = 0.24 \pm 0.05$ dex, and $v \sin i = 15.7 \pm 0.5\ {\rm km\ s^{-1}}$. We chose not to include the FEROS data in the RV modeling. All points fall near phases (−0.4, 0.025, and 0.35) where the RV signal is close to 0 and therefore do not meaningfully contribute while adding one instrument and the associated extra parameters. Using the CERES pipeline (Brahm et al. 2017a), we also recover chromospheric emission indices, tracers of stellar activity. The core emission of the H_α line at 6562.808 Å is $H_\alpha = 0.160 \pm 0.005$ (following Boisse et al. 2009). Using regions defined by Duncan et al. (1991) and calibrations from Noyes et al. (1984), we measure the core emission of the Ca II H and K lines around 3933 Å and 3968 Å to be $\log R'_{\rm HK} = -4.503 \pm 0.044$. This value is consistent with

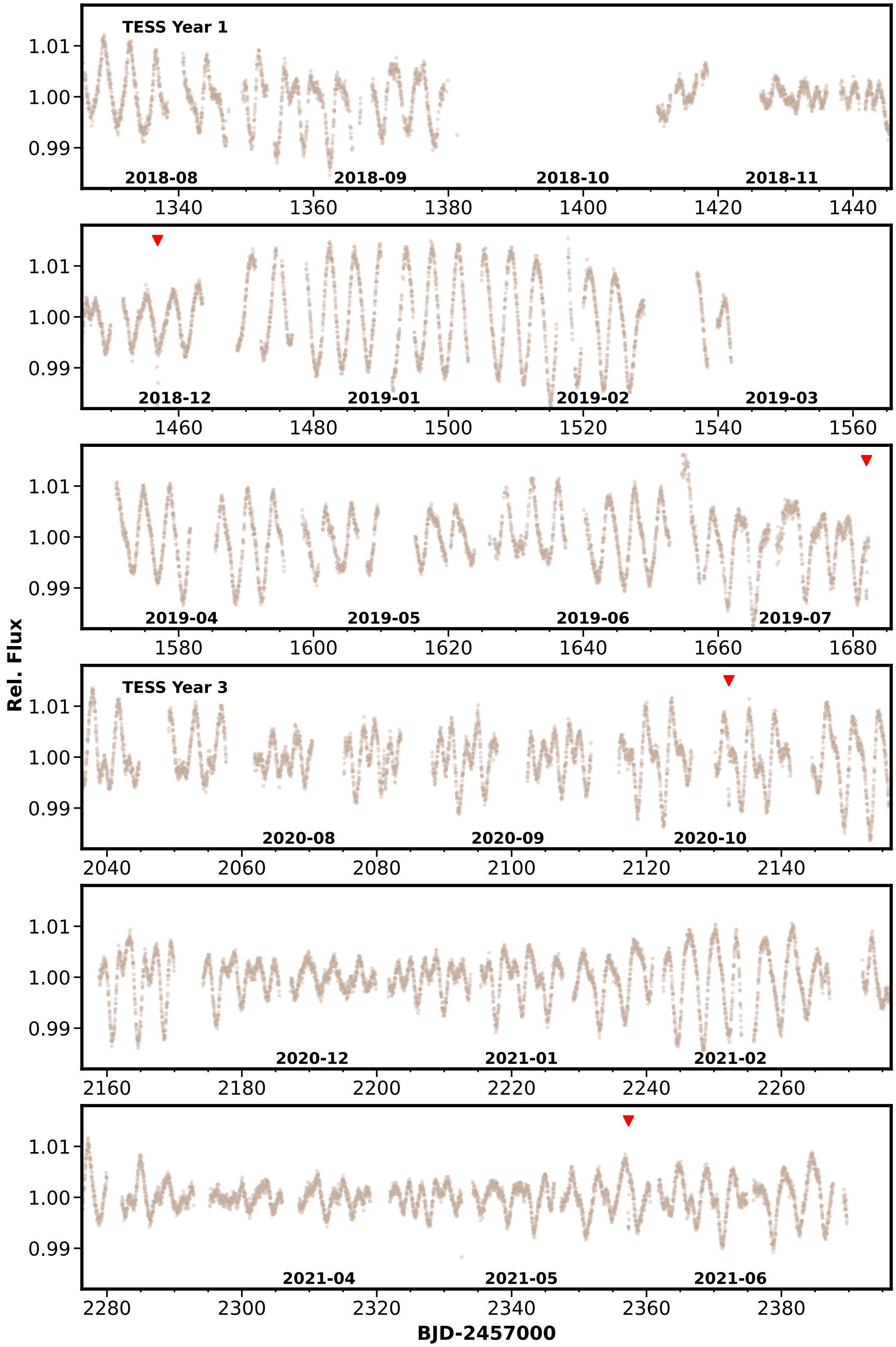

Figure 1. TESS light curve (brown) of TOI-4562b from all 25 available sectors. Photometry prior to sector 13 was obtained at 30 minute cadence, while latter observations were obtained at 2 minute cadence and binned in this figure to 30 minutes for clarity. The four TOI-4562b transits from Sectors 5, 13, 30, and 38 are marked by red arrows. The host star exhibits up to ∼3% peak-to-peak stellar rotational modulation due to its youth.

a young active star (Mamajek & Hillenbrand 2008). Finally, legacy spectra from the GALAH survey (Buder et al. 2021) found $T_{\mathrm{eff}} = 6034 \pm 77$ K, $\log g = 4.36 \pm 0.18$, $[\mathrm{M/H}] = 0.08 \pm 0.06$, and $v \sin i = 15.6 \pm 2.2$ km s^{-1}.

2.5. Gemini South and SOAR: High-resolution Direct Imaging

A first high-resolution image of TOI-4562 was obtained on 2022 March 17 with the Zorro Speckle camera on the 8.1 m

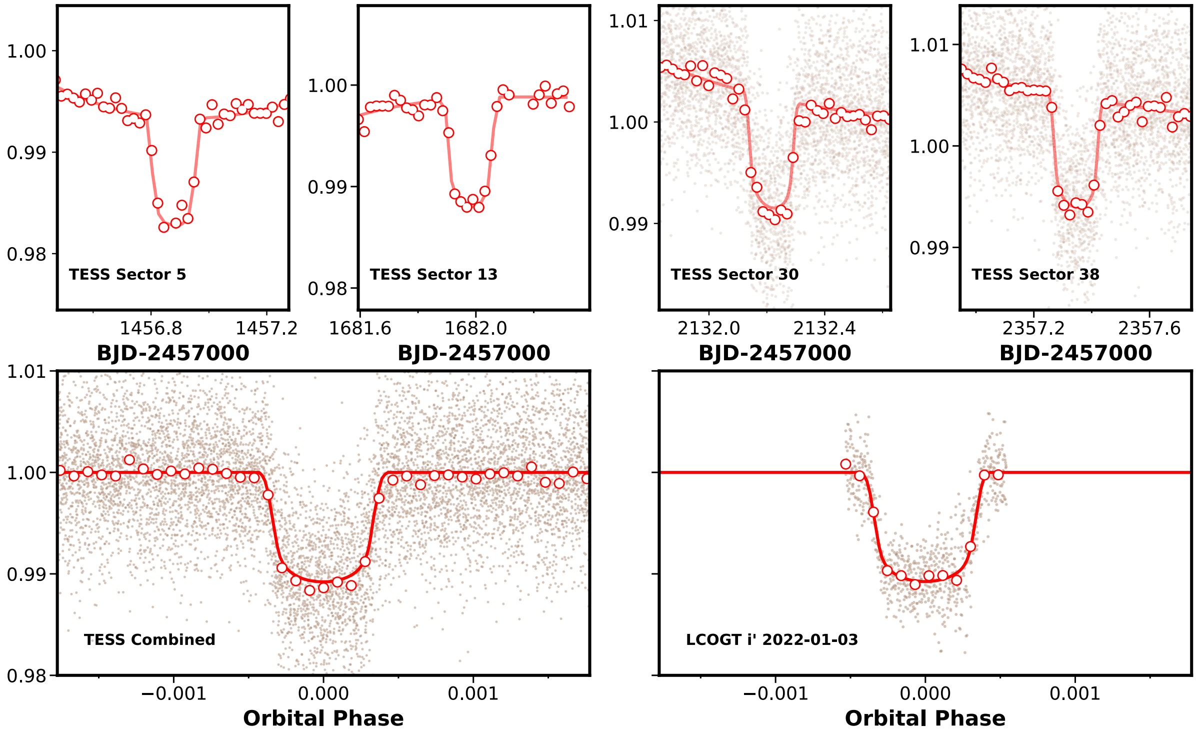

Figure 2. Top Individual transits from TESS from sectors 5 and 13 at 30 minute cadence and from sectors 30 and 38 at 2 minute cadence. The red circles indicate the measured data for sectors 5 and 13 and the binned data at 30 minute cadence for sectors 30 and 38. The 2 minute cadence data for sectors 30 and 38 are plotted as brown points. The best-fit model, incorporating the transit-timing variations in Section 4, and out-of-transit trends are shown by the red lines. Bottom left: the phase-folded TESS transit and best-fit model. Bottom right: the combined follow-up LCOGT 1 m observations from 2022 January 3 in the i' band.

Gemini South telescope (Howell & Furlan 2022) and is shown in the top panel of Figure 3. Simultaneous observations were obtained at 562 and 832 nm, respectively. Contrast curves were retrieved following Howell et al. (2011) for both wavelengths, and neither shows sign of a companion in the vicinity of TOI-4562b. A difference in magnitude Δm of 5 is achieved at a separation of $\sim 0\farcs1$. This allows us to rule out the presence of bright stellar objects in the same TESS pixel as TOI-4562 that would meaningfully impact the transit light curve to a projected distance of $\sim$35 au (given TOI-4562's distance of 350.0 ± 1.2 pc).

On 2022 April 19, another high-resolution image was acquired with the HRCam instrument on the 4.1 m SOAR telescope. TOI-4562 was observed as part of the SOAR TESS survey (Ziegler et al. 2020, 2021), and the data were reduced following Tokovinin (2018). The image shown in the bottom panel of Figure 3 and shows a contrast in the I band of 5 mag within $1''$ with no sign of a companion, in agreement with the Gemini South observation.

3. Age of TOI-4562

TOI-4562 does not appear in the extensive list of stars with known age and/or belonging to associations and moving groups compiled from the literature in Bouma et al. (2022). Similarly, we do not identify a coeval population when applying the COMOVE package (Tofflemire et al. 2021) that uses Gaia DR3 astrometric parameters to find whether a given possible young star candidate is comoving with its visual neighbors.

This lack of evidence of TOI-4562 belonging to any known moving group or open cluster means its age estimation is challenging. The variability seen in both photometry and radial velocity is indicative of the presence of rotationally modulated surface brightness features, likely due to the presence of dark spots and bright plages/faculae. Combined with a fast rotation period ($P_\star = 3.86^{+0.05}_{-0.08}$ days), this strongly suggests that TOI-4562 is a young and active star.

Determining the age of a field star is notoriously difficult (Soderblom 2010). In the following paragraphs, we make use of the rotation and lithium abundance of TOI-4562 to qualitatively assess its youth. We note that though TOI-4562 exhibits signatures of activity and youth indicative of being younger than 1 Gyr, pinpointing its age will remain difficult without placing it within comoving populations. With increasingly more sophisticated clustering with updated Gaia data sets, we hope that kinematics studies such as Oh et al. (2017), Gagne et al. (2018), Kounkel & Covey (2019), and Ujjwal et al. (2020) can provide improved census of young associations and groups.

3.1. Stellar Rotation and Gyrochronology

Young stars on the zero-age main sequence spin rapidly. Over the course of a few billion years, mass loss from stellar winds spin down Sunlike stars. The rotation period of Sunlike stars can be a tracer for their age. Rotation–color–age relationships such as those from Barnes (2007) and Mamajek & Hillenbrand (2008) are calibrated against coeval clusters and associations and can provide useful metrics to estimate stellar ages. Recent theoretically motivated models, which are based on wind-braking models and can incorporate core–envelope coupling, also provide such relationships (e.g., Spada & Lanzafame 2020).

The 25 sectors of observations gathered by TESS provide the means for a good estimation of the rotation period of TOI-4562. As shown in Figure 5, we ran the PYASTRONOMY

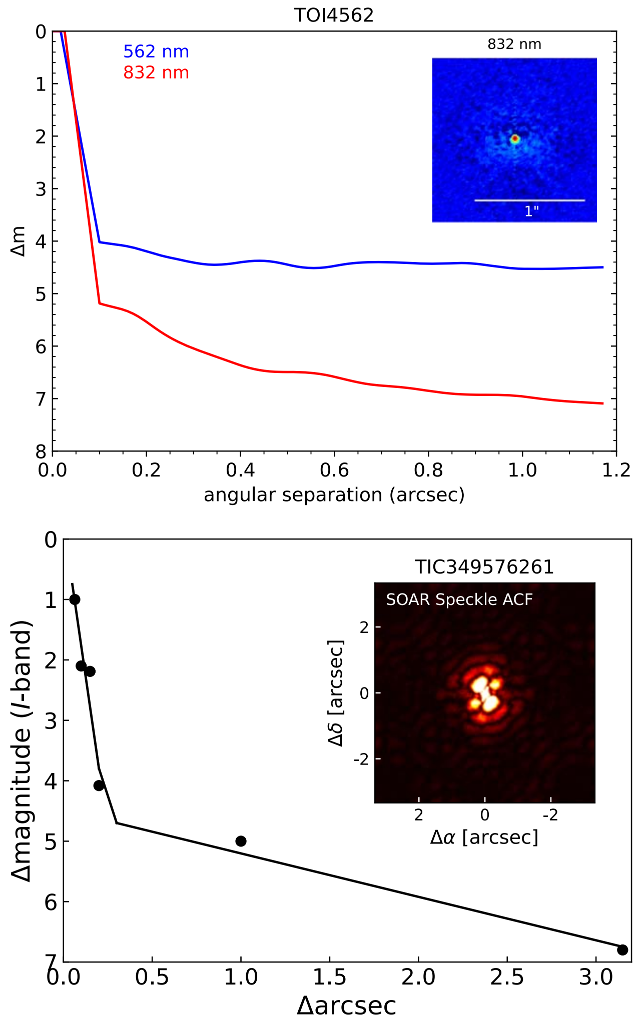

Figure 3. Top: high-resolution image of TOI-4562 obtained with the Zorro camera attached to the 8.1 m Gemini South telescope. The blue and red curves show difference in magnitude as a function of orbital separation from TOI-4562 obtained at wavelengths of, respectively, 562 and 832 nm. The inset plot shows the reconstructed image at 832 nm where no companion is detected. Bottom: SOAR HRCam high-resolution imaging of TOI-4562. The difference in magnitude as a function of orbital separation from TOI-4562 is shown by the black curve and the autocorrelation function on the inset image. There is no sign of a stellar-sized companion to TOI-4562.

implementation of the generalized Lomb–Scargle periodogram (GLS; Lomb 1976; Scargle 1982; Zechmeister & Kurster 2009) on the entire data set and measured a rotation period of $P_\star = 3.86^{+0.05}_{-0.08}$ days. To obtain $P_\star$, we first computed separate GLS periodograms for individual sectors (each covering $\sim$7 $P_\star$) previously binned to a 10 minute cadence. The median and 1σ values of all obtained periods were then used to derive $P_\star$ and the associated uncertainties.

We note the clear second periodogram peak in Figure 5, close to $P_\star$. This could be showing differential rotation (i.e., the variation of $P_\star$ as a function of stellar latitude). This has been largely observed in Kepler stars (Reinhold et al. 2013). We could suppose that the rotational modulation of two distinct clumps of surface stellar spots evolving at a different latitude would be at the origin of the double peak (Lanza et al. 1993).

In addition, TOI-4562 received 4 yr of monitoring with the Wide Angle Search for Planets (WASP) Consortium (Pollacco et al. 2006) Southern SuperWASP facility from 2008 to 2012. WASP-South is located at SAAO and consists of an array of eight commonly mounted 200 mm f/1.8 Canon telephoto lenses, each with a 2 K × 2 K detector. A period analysis of the WASP-South light curves reveals periods of 3.74, 3.84, 3.82, and 3.84 days for the 2008/2009, 2009/2010, 2010/2011, and 2011/2012, respectively, in agreement with the TESS light curves. The long-term stability of the signal helps to confirm it as the correct alias of the rotational modulation signal. We note that WASP did not cover any transit event.

Finally, we run periodograms on the available light curves from the All-Sky Automated Survey for Supernovae (ASAS-SN; Shappee et al. 2014; Jayasinghe et al. 2019). Sloan *g*-band data spanning from 2017 October to 2022 April show very strong peaks in the periodogram at 3.84, 3.87, and 3.82 days for the 2018/2019, 2019/2020, and 2020/2021 seasons, respectively (2017 and 2022 data sets are of poorer quality), agreeing with the other photometric data sets. The Johnson *V*-band data was obtained between October 2016 and September 2018. Despite being less extensive and less densely sampled than the *g*-band photometry, a moderate peak (FAP $\sim$ 0.2%) is found at 3.64 days, close to $P_\star$.

Using the age–rotation relationship from Mamajek & Hillenbrand (2008), we found TOI-4562b to be 110–490 (3σ) Myr old. We note that age estimates from this relationship assume that the star lies on the slow sequence of the age–rotation relationship. Stars are often found to be more rapidly rotating than such sequences for a given age, which has been attributed to binarity in cluster populations (e.g., Douglas et al. 2016; Gillen et al. 2020). Though there is no evidence for TOI-4562 being part of a binary system, caveats still apply for gyrochronology-based age estimates. For a 1.2 $M_\odot$ star with $P_\star = 3.86^{+0.05}_{-0.08}$, the model from Spada & Lanzafame (2020) gives a consistent age estimate of 300–400 Myr.

The top plot of Figure 6 shows the rotation period of TOI-4562 compared with stars of known nearby clusters and associations. TOI-4562's $P_\star$ is consistent with that of stars belonging to Group X (Messina et al. 2022; Newton et al. 2022), with an estimated age of 300 Myr.

3.2. Lithium

The convective envelope of low-mass stars ($M_\star < 1.5\ M_\odot$) allows efficient transport of lithium to deeper and hotter regions in a star's interior, where it gets destroyed by proton capture. Calibrated with stars in clusters and associations, this lithium depletion can be used as a proxy for stellar age. Using CHIRON spectra (see Section 2.3), we measured the equivalent width of the lithium doublet at 6707.76 and 6707.91 Å. We fit two Gaussian line profiles of the same depth at the respective wavelengths of the lithium doublet and one auxiliary with a different depth to account for the nearby Fe I line at 6707.43 Å usually blended with the Li doublet. All profiles share the same width as per the rotational broadening of the star. We measure a lithium equivalent width of 0.084 ± 0.007 Å from a median-combined spectrum of all our CHIRON observations. These data are displayed in Figure 6. On the same figure, we show the lithium equivalent width as a function of effective temperature for stars belonging to clusters with well-constrained ages, the Pleiades ($\sim$ 125 Myr), Group X ($\sim$ 300 Myr), and Praesepe ($\sim$ 670 Myr). TOI-4562 exhibits a Li equivalent width shallower than most of the Pleiades stars and of comparable strength to stars from the Praesepe cluster, at an effective temperature of 6000 K.

Table 1
TOI-4562 Parameters

Parameters	Description	Prior	Value	Reference
Name and position				
TOI	TESS Object of Interest	·	4562	
TIC	TESS Input Catalog	·	349576261	ST18
Gaia	DR2 Source ID	·	5288681857665822080	Gaia EDR3
R.A.	Right ascension (HH:MM:SS, J2000, epoch 2015.5)	·	07:28:02.41	Gaia EDR3
Decl.	decl. (DD:MM:SS, J2000, epoch 2015.5)	·	·63:31:04	Gaia EDR3
$\mu_{\mathrm{R.A.}}$	R.A. proper motion (mas yr^{-1})	·	·5.899 ± 0.015	Gaia EDR3
$\mu_{\mathrm{decl.}}$	decl. proper motion (mas yr^{-1})	·	10.491 ± 0.011	Gaia EDR3
Type	Spectral type	·	F7V	
ϖ	Parallax (mas)	$\mathcal{G}$[2.857, 0.05][a]	$2.85692^{+0.01009}_{-0.00990}$	This work
D	Distance (parsec)	·	350.0 ± 1.2	This work
Photospheric parameters				
T_{eff}	Effective temperature (K)	·	6096 ± 32 K	This work (CHIRON)
log g	Surface gravity (dex)	·	4.39 ± 0.01	This work
[M/H]	Bulk metallicity (dex)	$\mathcal{G}$[0.2, 0.3]	0.08 ± 0.06	This work
v sin i	Rotational velocity (km s^{-1})	·	17 ± 0.5	This work (CHIRON)
Physical parameters				
$M_\star$	Mass ($M_\odot$)	$\mathcal{U}$[0, 2]	1.192 ± 0.057	This work
$R_\star$	Radius ($R_\odot$)		1.152 ± 0.046	This work
Age	Age (Myr)		<700	This work
Activity parameters				
$P_\star$	Equatorial rotation period (days)	·	$3.86^{+0.05}_{-0.08}$	This work
Li 6708 EW	Li doublet (∼6708 Å) equivalent width (Å)	·	0.076 ± 0.022	This work
log R'_{HK}		·	·4.503 $^{+0.028}_{-0.052}$	This work (FEROS)
Photometric parameters				
$E(B\text{-}V)$	Interstellar extinction (mag)	$\mathcal{U}$[0, 0.1542][b]	<0.01 (3σ)	This work
T	TESST(mag)	·	11.533 ± 0.006	ST18
V	Johnson V(mag)	·	12.098 ± 0.014	H16
B	Johnson B (mag)	·	12.698 ± 0.025	H16
G	Gaia G(mag)	·	11.948 ± 0.020[c]	Gaia EDR3
B_{p}	Gaia B_{p}(mag)	·	12.262 ± 0.020[c]	Gaia EDR3
R_{p}	Gaia R_{p}(mag)	·	11.467 ± 0.020[c]	Gaia EDR3
J	2MASS J(mag)	·	10.931 ± 0.023	SK06
H	2MASS H(mag)	·	10.693 ± 0.025	SK06
K_{s}	2MASS K_{s}(mag)	·	10.619 ± 0.023	SK06
W_1	WISE W_1(mag)	·	10.578 ± 0.023	W10,C13
W_2	WISE W_2(mag)	·	10.618 ± 0.020	W10,C13
W_3	WISE W_3(mag)	·	10.590 ± 0.061	W10,C13
NUV	GALEX/NUV calibrated AB magnitude (mag)	·	17.133 ± 0.023	B17

Notes.
[a] Adopted from Gaia EDR3 Gaia Collaboration et al. (2016, 2021), corrected using a zero-point offset value of −0.024 mas, following Lindegren et al. (2021a).
[b] Adopted from Schlafly & Finkbeiner (2011).
[c] These are inflated uncertainties from the Gaia photometric bands, following the convention from Eastman et al. (2013). Priors: $\mathcal{U}$ a, b uniform priors with boundaries a and b; $\mathcal{G}[\mu,\sigma]$ Gaussian priors.
References. (Gaia EDR3) Gaia Collaboration et al. (2016, 2021); (ST18) Stassun et al. (2018); (SK06) Skrutskie et al. (2006); (W10) Wright et al. (2010); (C13) Cutri et al. (2021); (B17) Bianchi et al. (2017); (H16) Henden et al. (2016).

Combined with the gyrochronology analysis, TOI-4562's age is consistent with a star younger than the Praesepe/Hyades clusters (i.e., $\lesssim$700 Myr).

3.3. Lithium, log R'_{HK}, and B − V

Finally, we used the more recent BAFFLES package (Stanford-Moore et al. 2020) to derive an age estimate. BAFFLES is a Bayesian framework in which lithium abundance, the log R'_{HK} index, and $B-V$ color are used to infer an age posterior for the studied star. The likelihood functions used are calibrated against stars belonging to open clusters and associations (i.e., with well-constrained ages). For log R'_{HK}=−4.503 (from the FEROS spectra), Li 6708 EW = 84 ± 7 mÅ, and $B-V=0.52\pm0.03$ (corrected from extinction), we recover a 1σ age estimate of 340-715-1500 Myr. This is slightly higher than our previous estimate, but we note that BAFFLES uses an age posterior extending by default to 12 Gyr. Compared to the star sample used in Morris (2020) belonging to well-studied star clusters, TOI-4562's photometric variability and rotation period are respectively larger and smaller than any stars of age 1 Gyr, therefore pointing to a younger age. Applying a conservative maximum age cutoff of 1.5 Gyr to the age posterior when running BAFFLES yields a 1σ age of 320-619-1100 Myr, closer to previously quoted values.

All parameters for TOI-4562 are summarized in Table 1.

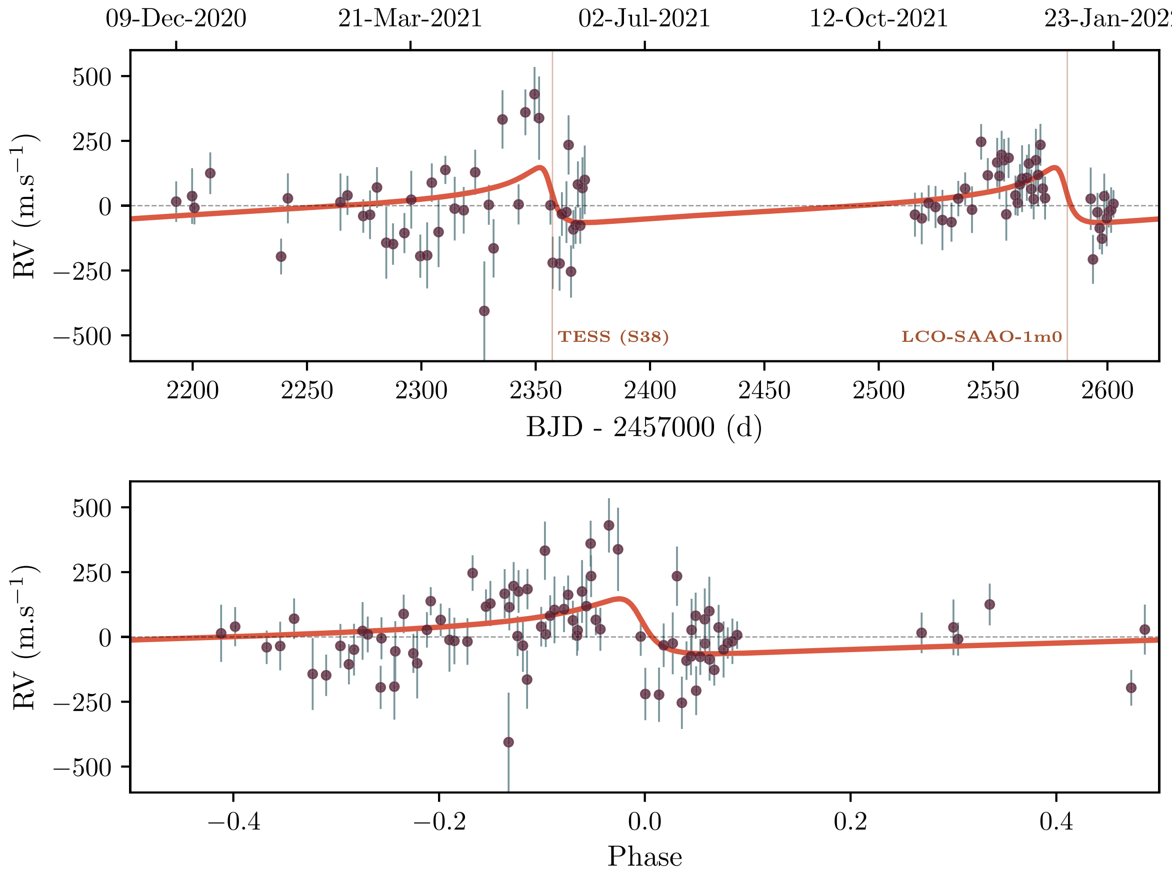

Figure 4. Top: 2 yr radial-velocity time series of TOI-4562 obtained with the CHIRON spectrograph (brown circles) with the associated error bars. The Keplerian orbit fit from our global modeling is shown by a red line. Transits are highlighted in light brown. Bottom: phase-folded RVs (brown circles) with the Keplerian orbit best fits shown by a red line.

4. Analysis and Results

To best determine the system properties of TOI-4562, we perform a joint modeling of all available photometric and spectroscopic data sets, including stellar isochrone models that constrain the properties of the host star. The remainder of Section 4. detail individual components of this model.

4.1. Transit Modeling

Despite the 225 day orbital period of TOI-4562b, the extensive observations of TOI-4562 by TESS allowed four transits to be observed. Spot-modulated variability at the ∼3% level is seen on the TESS light curve due to the active nature of TOI-4562, as expected given its young age. For the purposes of the transit modeling, we detrend the region around each transit epoch with a fourth-order polynomial. The polynomial is fitted using the out-of-transit regions of the light curve within 0.5 days of the transit center. We model the transits as per Mandel & Agol (2002) via the BATMAN package (Kreidberg 2015). Free parameters that describe the transit model include the transit center T_c at each transit epoch, radius ratio $R_p/R_\star$, line-of-sight inclination of the transit i, and the eccentricity parameters $\sqrt{e}\cos\omega$ and $\sqrt{e}\sin\omega$. A quadratic model was used to account for limb darkening using coefficients $\mu_{1\mathrm{TESS}}$ and $\mu_{2\mathrm{TESS}}$, fixed to those interpolated from Claret (2017) at the atmospheric parameters of TOI-4562 for the TESS transits. We note that $a/R_\star$ was not directly sampled but rather computed from the free parameters P_{orb}, $M_\star$, $R_\star$ and planet mass M_p. For the two (same epoch, different telescopes) SAAO LCOGT transits, the limb-darkening coefficients $\mu_{1_{\mathrm{LCO}}}$ and $\mu_{2_{\mathrm{LCO}}}$ are computed for the SDSS i' band from Claret & Bloemen (2011), using the interpolation routine from Eastman et al. (2013) with $T_{\mathrm{eff}} = 6000$ K, log $g = 4.5$, and [M/H] = 0.1, computed with the least-squares method (LSM). For the SAAO LCOGT data, we also incorporate the effects of instrumental systematic variations that are common to ground-based photometric observations via a simultaneous detrending of the light curve against parameters describing the observation air mass to which we add a linear trend with respect to time. All detrended light curves and the best transit-model fits are shown in Figure 2.

4.2. Eccentric Orbit Validation

Even though the transit shape points to a very eccentric orbit, this can be degenerate with the mean stellar density $\rho_\star$. To cross-validate the eccentric nature of TOI-4562b's orbit, we compared the stellar density obtained from isochrone fitting, which we call $\rho_\star$, to the stellar density obtained from a forced circular orbit, which we call ρ_{circ}. To obtain ρ_{circ}, we run a transit-only model, imposing $e = 0$ and with the following free parameters: ρ_{circ}, transit center T_c for each transit, radius ratio $R_p/R_\star$, impact parameter b, limb-darkening coefficients ($\mu_{1_{\mathrm{LCO}}}$, $\mu_{2_{\mathrm{LCO}}}$, $\mu_{1_{\mathrm{TESS}}}$ and $\mu_{2_{\mathrm{TESS}}}$), and instrument systematics parameters (for the SAAO LCOGT transits). Leveraging this photoeccentric effect (Dawson et al. 2012) allows us to recover the space of possible parameters for e and w (see Dawson et al. 2015). On Figure 8, we show in blue the resulting 2D

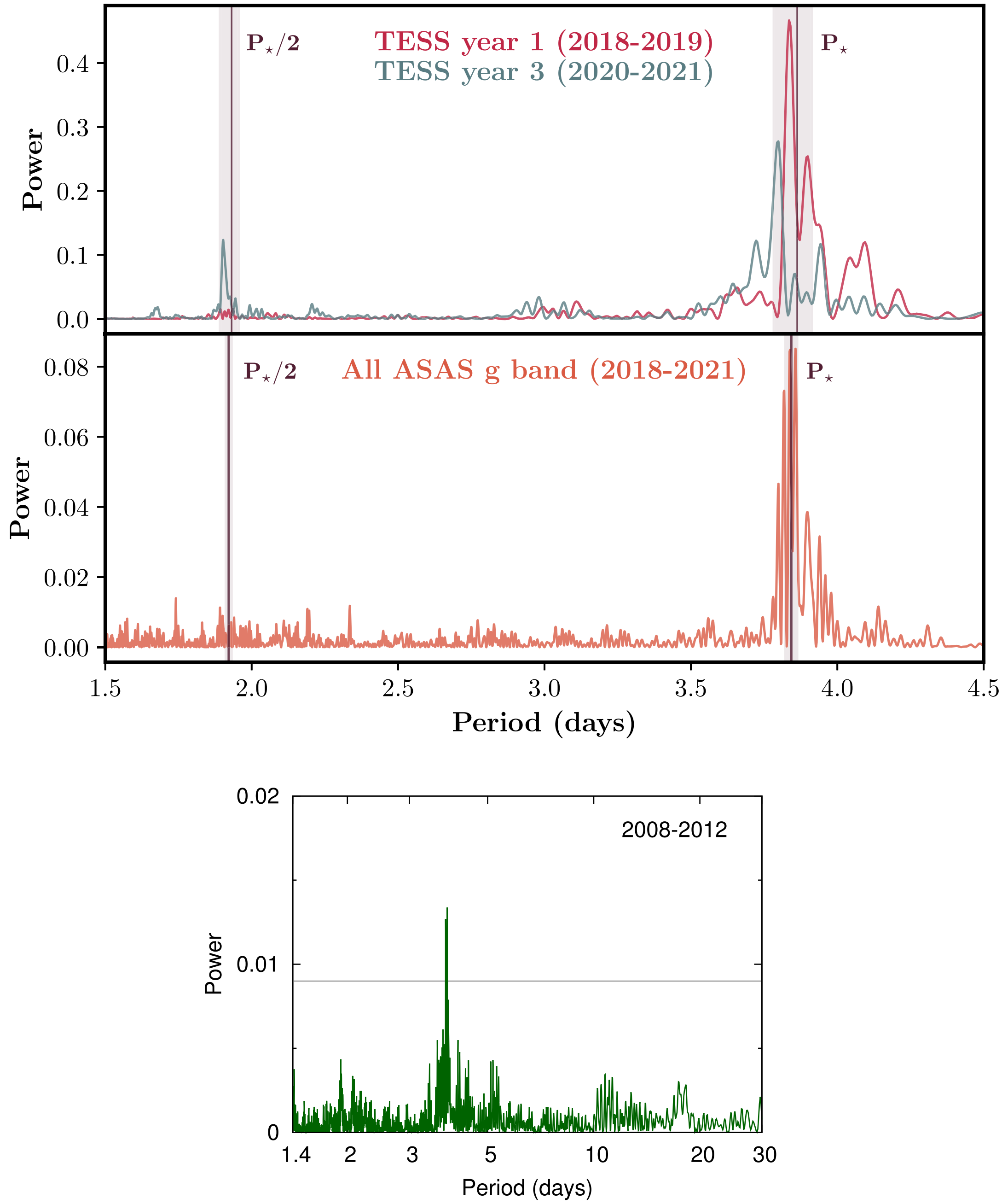

Figure 5. Top: GLS periodogram of TOI-4562's photometry from TESS for the first (2018–2019; red line) and third (2020–2021; blue line) year of data. The identified stellar rotation period ($P_\star = 3.86^{+0.05}_{-0.08}$) and the first harmonic ($P_\star/2$) are shown with the vertical brown lines, with the surrounding shaded areas representing uncertainties. Middle: GLS periodogram of ASAS-SN's photometry gathered between 2018 and 2021 (orange line). The identified stellar rotation period ($P_\star = 3.84 \pm 0.02$) and the first harmonic ($P_\star/2$) are shown as the vertical brown lines with their respective uncertainties (shaded area). Bottom: Periodogram on the 4 yr (2008–2012) of WASP data yielding $P_\star$ estimates between 3.74 and 3.84, depending on the considered year. In all three periodograms, we notice a strong peak multiplicity around 3.9 days that could be associated with stellar surface features tracing differential rotation.

distribution of e and w that agree with the derived ratio for $\rho_{\rm circ}/\rho_\star$, given[40] :

$$\frac{\rho_{\rm circ}}{\rho_\star} = \frac{(1 + e\,\sin w)^3}{(1 - e^2)^{3/2}}. \tag{1}$$

This grants us increased confidence of the true eccentric nature of TOI-4562b's orbit.

[40] In the case of TOI-4562b, the condition $\left(\frac{a}{R_\star}\right)^2 \gg \frac{2}{3}\left(\frac{1+e}{1-e}\right)^3$, required for 1 to be valid (see Kipping 2014), is fulfilled.

4.3. Radial-velocity Modeling

The radial velocities obtained over the two consecutive orbits of TOI-4562b were modeled using a Keplerian orbit. Some fitted parameters are shared with the transits and stellar isochrone fitting, such as T_c, $P_{\rm orb}$, $a/R_\star$(derived), $R_\star$, $M_\star$, i, $\sqrt{e}\cos\omega$, and $\sqrt{e}\sin\omega$. To model the velocities, we add the planet mass M_p, a radial-velocity offset $\gamma_{\rm rel}$, and a white-noise term, σ_{Y1}. The semiamplitude of the planetary signature $K_{\rm amp}$ was computed from the above parameters. The orbital solution and the associated likelihood from the fit to the data

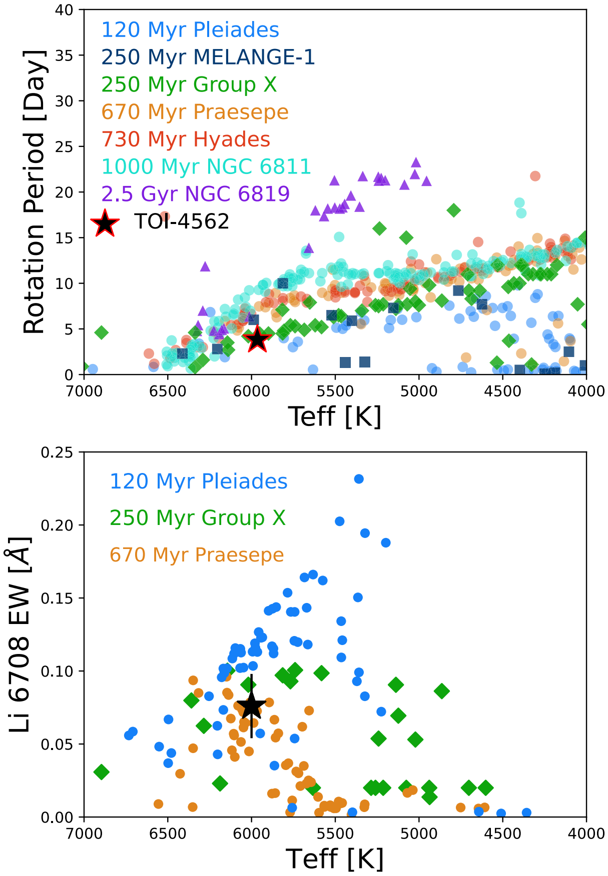

Figure 6. Youth indicators for TOI-4562. Top: the rotation period of TOI-4562 compared to the distribution of stars within known associations and clusters, including the Pleiades (Rebull et al. 2016), MELANGE-1 (Tofflemire et al. 2021), Group X (Messina et al. 2022; Newton et al. 2022), Praesepe and Hyades (Douglas et al. 2016, 2019), NGC 6811 (Curtis et al. 2019), and NGC 6819 (Meibom et al. 2015). Bottom: equivalent width of the lithium doublet at 6707.76 and 6707.91 Å for TOI-4562 (black star) and stars in the Praesepe (orange circles; Cummings et al. 2017), Group X (green diamonds; Newton et al. 2022), and Pleiades (blue circles; Bouvier et al. 2018) clusters. TOI-4562 lies at an age comparable to the Hyades and Praesepe.

are computed from K_{amp}, T_c, P_{orb}, $\sqrt{e}\cos\omega$, and $\sqrt{e}\sin\omega$ via the RADVEL package (Fulton et al. 2018).

We also try to add a Gaussian process using a quasiperiodic kernel, implemented through RADVEL to model the stellar noise apparent in the data. The resulting parameter values do not yield a significant difference, therefore not justifying the necessity to use a correlated noise model to account for the stellar intrinsic variability seen in the radial velocities. With one data point a day at most, the sampling is too sparse for the Gaussian process to correctly grasp the ∼4 day stellar period. Crudely assuming a spot covering 0.6%–1.2% (δ_{spot}) of the stellar surface, we can approximate an activity-induced radial-velocity semiamplitude K_{act} of $v\sin i \times \delta_{\mathrm{spot}} \sim 100$–$200$ m s^{-1}, comparable to the jitter level seen in Figure 4.

We attempted to fit a second longer-period circular planet to the radial velocities. We used uniform priors for the period ($\mathcal{U}$[300: 2000] days), planet mass ($\mathcal{U}$[0.002: 0.1] $M_\odot$), and t_0 ($\mathcal{U}$[1398: 3398] TESS Barycentric Julian Date). The posterior distributions are not clearly converging, favoring larger periods and smaller masses. With a K_{amp} of ∼70 m s^{-1}, the best solution is clearly below the activity level and therefore not trustworthy. Long-term data is needed to attempt to constrain a longer-period companion.

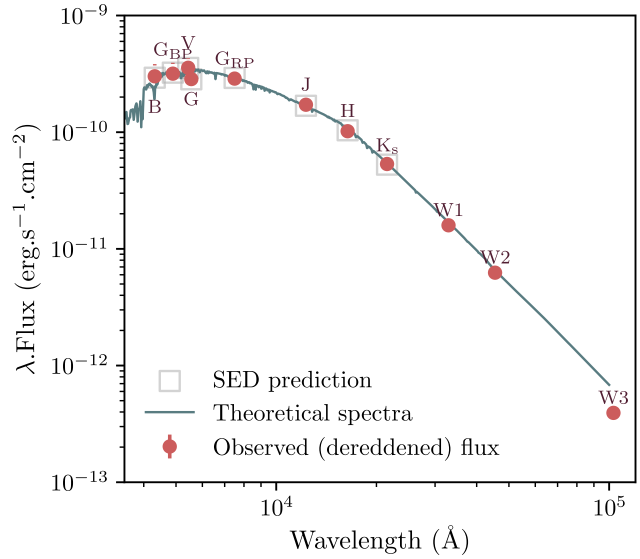

Figure 7. SED of TOI-4562 b. Red points are the observed magnitudes in different wavelength bands (labeled with corresponding letters) corrected from interstellar reddening. Predicted magnitudes from the isochrone part of our global model are shown as gray open squares. The gray line is a theoretical spectra for a star with $T_{\mathrm{eff}} = 6000$ K, $\log g = 4.5$ dex, and [M/H] = 0 (adopted from Coelho 2014).

4.4. Spectral Energy Distribution Model

To constrain the host star parameters $R_\star$, $M_\star$, [M/H], and T_{eff} we also model the spectral energy distribution (SED) of TOI-4562 simultaneously to the transit and radial-velocity models. The stellar parameters are modeled using the MESA Isochrones and Stellar Tracks (Paxton et al. 2011, 2013, 2015; Choi et al. 2016). We interpolate evolution tracks using the MINIMINT package (Koposov 2021) against $M_\star$, age, [M/H], and the photometric bands B, V, Gaia G, Bp, Rp, and 2MASS bands J, H, and K. $R_\star$ is derived from the isochrone-predicted values for $\log g$ and $M_\star$. To account for uncertainties in the stellar evolution models, we adopt a 4% uncertainty floor in stellar radius and 5% floor in stellar mass, where appropriate (Tayar et al. 2022). For the effective temperature T_{eff}, we apply a Gaussian prior such that the predicted T_{eff} interpolated from the isochrone is compared against that measured from the CHIRON spectra as an additional likelihood term. Predicted fluxes from the SED model are corrected for interstellar reddening with the PYASTRONOMY UNRED package, which uses the parameterization from Fitzpatrick (1999). Extinction is a free parameter, with a maximum value of $E(B-V) = 0.1542$ mag, as estimated from the Schlafly & Finkbeiner (2011) maps over a 5′ radius[41] around TOI-4562. We also incorporate a Gaussian prior on the distance modulus via the observed Gaia parallax to TOI-4562. We offset Gaia DR3's parallax value by −0.023861 mas, the parallax zero-point offset estimated using the routine from Lindegren et al. (2021a),[42] and function of ecliptic latitude, magnitude, and color. At each Markov Chain Monte Carlo (MCMC) jump step, the observed SED is compared against the interpolated MIST model predictions for a given tested stellar parameter.

[41] Obtained from the NASA/IPAC Infrared Science Archive.
[42] https://gitlab.com/icc-ub/public/gaiadr3_zeropoint

Table 2
TOI-4562b Parameters

Parameters	Description	Priors	Values
Transit parameters			
$T_{c,1}$ [a]	Transit mid-time (BJD_{TDB})	$\mathcal{U}$[1456.83,1456.93]	$1456.87991^{+0.00142}_{-0.00120}$
$T_{c,2}$ [a]	Transit mid-time (BJD_{TDB})	$\mathcal{U}$[1681.94,1682.04]	$1681.98324^{+0.00136}_{-0.00142}$
$T_{c,3}$ [a]	Transit mid-time (BJD_{TDB})	$\mathcal{U}$[2132.17,2132.27]	$2132.21577^{+0.00088}_{-0.00095}$
$T_{c,4}$ [a]	Transit mid-time (BJD_{TDB})	$\mathcal{U}$[2357.29,2357.39]	$2357.34544^{+0.00079}_{-0.00080}$
$T_{c,5}$ [a]	Transit mid-time (BJD_{TDB})	$\mathcal{U}$[2582.41,2582.51]	$2582.46321^{+0.00142}_{-0.00036}$
T_c [a]	Derived linear ephemeris	$\mathcal{U}$[1456.83,1456.93]	$1456.87168^{+0.00101}_{-0.00101}$
P_{orb} [a]	Orbital period (days)	Derived linear ephemeris	$225.11781^{+0.00025}_{-0.00022}$
T_{14}	Transit total duration (hours)	·	4.32 ± 0.04
$R_p/R_\star$	Radius ratio	$\mathcal{U}$[0, 0.2]	$0.09980^{+0.00084}_{-0.00092}$
$a/R_\star$	Normalized semimajor axis, derived from [$M_\star$,$R_\star$,P_{orb},M_p]	·	$147.4^{+1.44}_{-1.26}$
b	Impact parameter	·	$0.60^{+0.03}_{-0.04}$
δ	Transit depth (ppm)	·	9961^{+167}_{-184}
$\sqrt{e}\cos\omega$ [a]	Reparameterization of e and ω	$\mathcal{U}[-1, 1]$	$0.442^{+0.110}_{-0.131}$
$\sqrt{e}\sin\omega$ [a]	Reparameterization of e and ω	$\mathcal{U}[-1, 1]$	$0.752^{+0.058}_{-0.063}$
i	Planet orbit inclination (°)	$\mathcal{U}$[84, 90]	89.06 ± 0.04
$\mu_{1_{TESS}}$ [b]	Quadratic limb-darkening law coefficient 1 (TESS)	Fixed	0.28
$\mu_{2_{TESS}}$ [b]	Quadratic limb-darkening law coefficient 2 (TESS)	Fixed	0.29
$\mu_{1_{LCO}}$ [c]	Quadratic limb-darkening law coefficient 1 (LCO)	Fixed	0.28
$\mu_{2_{LCO}}$ [c]	Quadratic limb-darkening law coefficient 2 (LCO)	Fixed	0.29
Radial velocities parameters			
K	RV semiamplitude (m s^{-1})	-	106^{+24}_{-26}
M_p	Mass ($M_\odot$)	$\mathcal{U}$[0, 0.2]	0.0022 ± 0.0005
γ_{CHIRON}	RV offset (m s^{-1})	$\mathcal{U}$[5200, 5400]	5347 ± 13
σ_{Y1}	RV jitter, first orbit (m s^{-1})	$\mathcal{U}$[0, 600]	73^{+15}_{-15}
Derived parameters			
R_p	Radius ($R_\oplus$)	·	12.53 ± 0.15
	Radius (R_J)	·	$1.118^{-0.014}_{+0.013}$
M_p	Mass ($M_\oplus$)	·	732^{+152}_{-149}
	Mass (M_J)	·	$2.30^{+0.48}_{-0.47}$
e	Eccentricity	·	$0.76^{+0.02}_{-0.02}$
w	Argument at periapse (°)	·	60^{+9}_{-8}
ρ_p	Density (g cm^{-3})	·	$2.06^{+0.42}_{-0.44}$
a	Semimajor axis (au)	·	$0.768^{+0.005}_{-0.005}$
$\langle T_{eq}\rangle$	Temporal average equilibrium temperature (K)[d]	·	318 ± 4
T_{peri}	Equilibrium temperature at periapsis (K)	·	717^{+29}_{-37}
T_{apo}	Equilibrium temperature at apoapsis (K)	·	262^{+3}_{-2}

Notes. Priors: $\mathcal{U}$ [a, b] uniform priors with boundaries a and b.
[a] Parameters common to the transit and RV models.
[b] Adopted form the TESS band from Claret (2017), using ATLAS model with $T_{eff} = 6000$ K, log $g = 4.5$, and [M/H] = 0.1 and computed with the LSM.
[c] Computed for the SDSS i' band from Claret & Bloemen (2011), using the interpolation routine from Eastman et al. (2013) with $T_{eff} = 6000$ K, log $g = 4.5$, and [M/H] = 0.1 and computed with the LSM.
[d] Computed for an elliptical orbit from Mendez & Rivera-Valentin (2017), using an albedo of $A = 0.4$, $\epsilon = 1$, and $\beta = 0.74$.

4.5. Global Model

The global model includes simultaneous fits of the TESS and ground-based photometric data sets (4.1), the CHIRON velocities (4.3), and stellar isochrone model (4.4), as shown in Figures 2, 4, and 7, respectively. We explore the best-fit parameters and the posterior distribution via the affine invariant MCMC ensemble sampler EMCEE (Foreman-Mackey et al. 2013). The resulting parameters for TOI-4562b are given in Table 2.

Figure 8 illustrates the contribution of each part of the model to constrain the high eccentricity of TOI-4562b. In gray we show the distribution stemming from the value of $\rho_\star$ when imposing a circular orbit to the planet and fitting only for transits (see Section 4.2). Then, a model containing both the transits and isochrones, shown in red, greatly constrain the eccentricity. Finally, the addition of RVs (shown in yellow) only slightly improves the constraint of the eccentricity, due to both the large stellar activity and the poor coverage of the periastron passages.

5. Discussions and Conclusions

We report the discovery of TOI-4562b, a temperate gas giant on a highly eccentric orbit around a young Sunlike star. The planet has a mass of $2.30^{+0.48}_{-0.47}$ M_J and a radius of $1.118^{-0.014}_{+0.013}$ R_J. With an orbital period of $225.11781^{+0.00025}_{-0.00022}$ days, it is to date the second longest-period planet in the TESS sample (after

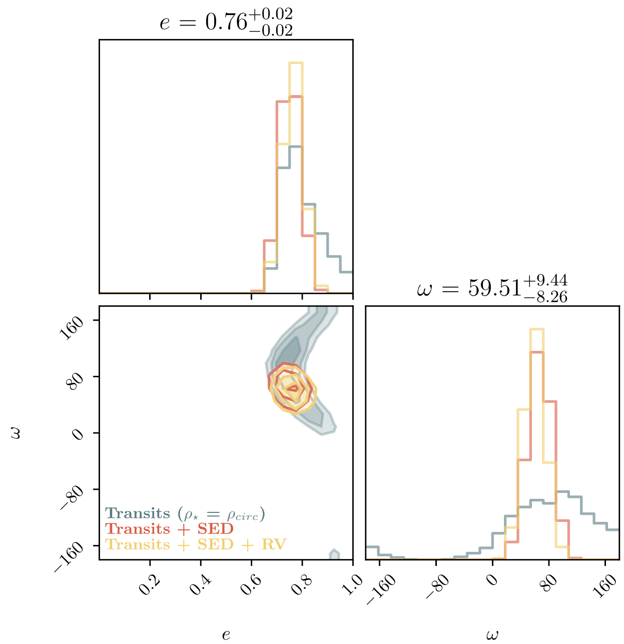

Figure 8. Posterior distributions for TOI-4562 b's orbital eccentricity (e) and argument at periapse (ω). The gray distribution was obtained from comparing $\rho_\star$ obtained from an SED fit and $\rho_{\rm circ}$ resulting from a fit of only the photometric data (TESS + LCO-SAAO) with an imposed circular orbit. The red and yellow posterior distributions, respectively, results from a photometric data + SED fit and the complete model including the radial velocities. .

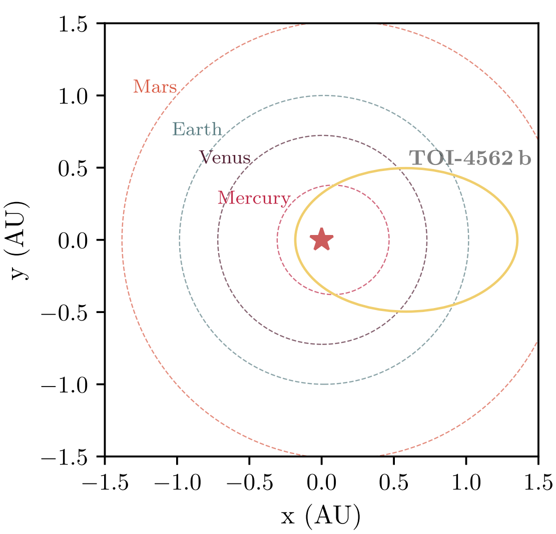

Figure 9. Two-dimensional orbit of TOI-4562b (yellow solid line) compared with Mercury (red dashed line), Venus (purple dashed line), Earth (blue dashed line), and Mars (orange dashed line).

TOI-2180b; Dalba et al. 2022). TOI-4562b resides in a highly elliptic orbit ($e = 0.76^{+0.02}_{-0.02}$) and has, based on (Spada & Lanzafame 2020), an age younger than the Praesepe and Hyades clusters. A representation of its orbit alongside the inner solar system planets is shown in Figure 9.

5.1. Radius Evolution

At the end of their accretion phase, newly formed gas giants are expected to have radii larger than 1 $R_{\rm J}$. As the planet core radiates its primordial internal heat, Jovian mass planets will cool down via the Kelvin–Helmholtz contraction to $\sim$1 $R_{\rm J}$. Only hot Jupiters, orbiting extremely close to their parent star, are expected to remain inflated due to their increased irradiation. According to cooling models (Baraffe et al. 2003; Fortney et al. 2007; Baraffe et al. 2008; Linder et al. 2019), shown in Figure 10, the most drastic changes in radius occur at the earliest ages. Measuring radii of young gas giants like TOI-4562b is therefore essential to set constraints on these such models, as emphasized in Fortney et al. (2007).

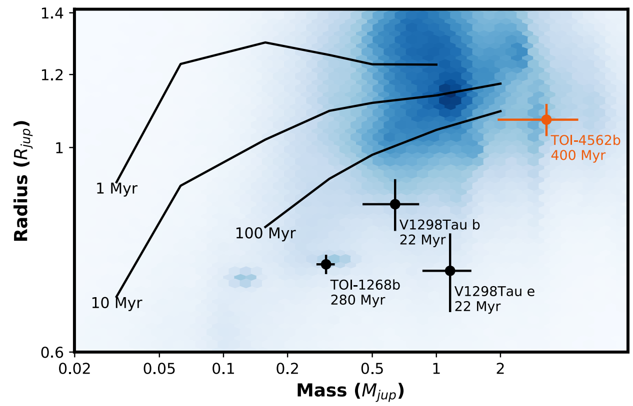

Figure 10. Young gas giants can help constrain the cooling and contraction models. To date, TOI-4562b is only the fourth Jovian planet younger than 500 Myr to have both its mass and radius measured. The mass–radius of TOI-4562b is plotted in orange alongside the planets in the V1298 Tau (David et al. 2019a; Suárez Mascareño et al. 2022) and TOI-1268 (Dong et al. 2022; Šubjak et al. 2022) systems. Unlike others, TOI-4562b sits along the isochrone tracks that model the contraction of young planets (Linder et al. 2019). The mass–radius distribution of other known planets are shown with a density plot in blue in the background.

The current picture is unclear as the recently measured mass of V1298 Tau b & e (Suárez Mascareño et al. 2022) yield much denser planets than predicted at 20 Myr old and require dramatic heavy element enrichment to somewhat reconcile with cooling models (see Figure 10). Conversely, TOI-4562b's radius is as expected for its age. At the closest approach to its host star ($\sim$0.18 au), it receives stellar irradiation of $\sim 9.3 \times 10^4$ W m^{-2}, or $\sim$68 times that of Earth. Although above the $\sim 1.6 \times 10^4$ W m^{-2} threshold to trigger inflation, given by Sestovic et al. (2018) for planets more massive than 2.5 $M_{\rm J}$, TOI-4562b's orbital eccentricity means this level of irradiation affects the planet for a very short fraction of the orbit, not sufficient to trigger radius inflation.

5.2. Dynamical History of TOI-4562 b and Benefits of Additional Follow-up

In its current observed state, TOI-4562b's semimajor axis and eccentricity (see Figure 11) are not in favor of a high-eccentricity migration scenario as a circularization of its orbit would take orders of magnitudes longer than the age of the universe ($\tau_{\rm circ} \sim 1 \times 10^7$ Gyr; Goldreich & Soter 1966). It is possible, however, that the planet is experiencing ongoing eccentricity cycles and we happen to be observing it at a lower eccentricity. Reduction of the star–planet distance at the periastron at the eccentricity peak of such cycles might allow the circularization process to be triggered as described in Dong et al. (2014). Disk–planet interactions can in principle excite the eccentricity of the orbit (Duffell & Chiang 2015), but this is restricted to low ($e \lesssim 0.2$) values, as shown with the red area in Figure 11. Debras et al. (2021) proposed that migration inside

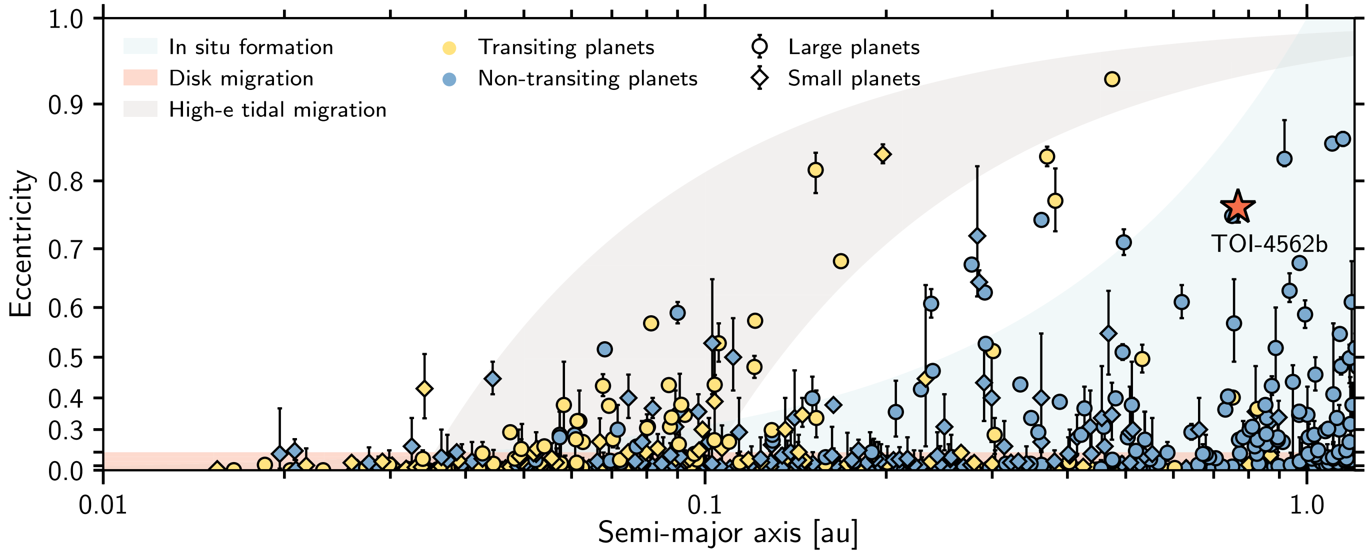

Figure 11. Eccentricity vs. semimajor axis for all confirmed planets (obtained from the NASA Exoplanet Archive 2022 February 13) with $M_p < 13\,M_J$. The vertical coordinate is scaled to e^2 to emphasize noncircular planets. Shaded areas highlight different formation scenarios. Planets in the gray region are on the path of high-eccentricity migration, with a final semimajor axis between 0.034 and 0.1 au. The upper and lower bounds of this region are set by the Roche limit and the circularization timescale, respectively. Disk migration, expected to only marginally excite orbital eccentricity, is shown as the red shaded region. Finally, in situ formation, with eccentricity excited by, e.g., planet–planet scattering, is shown as the blue shaded area. Transiting vs. nontransiting planets are labeled in yellow and blue symbols, respectively. Circles are representing larger ($R_p > 6\,R_\oplus$ and/or $M_p > 100\,M_\oplus$) planets, and diamonds are representing smaller planets ($R_p < 6\,R_\oplus$ and/or $M_p < 100\,M_\oplus$). Only planets with $e \geqslant 0.2$ and with uncertainties on e smaller than 50% of the measured e or planets with $e < 0.2$ and with uncertainties less than 0.2 are shown.

wide gaps carved in protoplanetary disks could result in gas giants with eccentricities up to 0.4. This is still insufficient to explain the very high eccentricity from TOI-4562b's orbit.

Another possible scenario to account for TOI-4562b's very high eccentricity is in situ formation (or alternatively, smooth disk migration), followed by excitation from a companion. This can occur via secular interactions or slow angular momentum exchanges with another body located further out, either periodically through, e.g., von Zeipel–Lidov–Kozai cycles (von Zeipel 1910; Kozai 1962; Lidov 1962; Nagasawa et al. 2008; Naoz 2016), or chaotically in secular chaos (Wu & Lithwick 2011; Hamers et al. 2017). High eccentricity can also be triggered sporadically in planet–planet scattering (Weidenschilling & Marzari 1996; Rasio & Ford 1996; Ford & Rasio 2006; Chatterjee et al. 2008) or stellar flybys (Shara et al. 2016; Rodet et al. 2021). Planet–planet scattering could have happened quickly and potentially early if triggered by the dissipation of the gas disk or if the planets were initially closely spaced. Constraints on an outer companion (if not ejected as a result of scattering) could provide crucial insights on dynamical evolution timescales, given the young age of the system.

The five transits of TOI-4562b show modest deviation from a linear ephemeris fit on the 5–20 minute level (see Figure 12). This potential detection of a transit-timing variation signal suggests the presence of a companion in the system, to which TOI-4562b probably owes its high eccentricity. The existing data are not sufficient to set meaningful constraints on the companion, and most configurations for period (i.e., inner or outer companion), eccentricity, and mutual inclination remain possible. TOI-4562b will be observed by TESS again in its second extended mission in 2023. In Table 3, we show future opportunities to continue monitoring transits of TOI-4562b in the years to come. Combining these with long-term radial-velocity follow-up might enable us to unravel the 3D architecture and dynamical history of this system, as has been

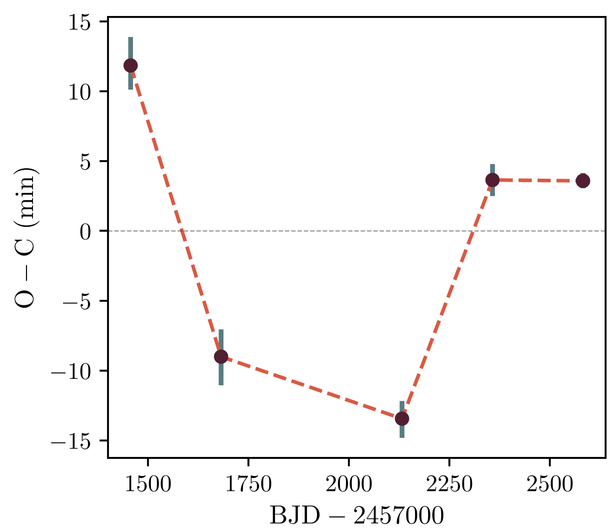

Figure 12. Observed—calculated midtransit time for the five transits of TOI-4562b, in minutes. The second and third transits (from TESS Sectors 13 and 30) show a ∼20 minute midtransit time difference with the other transits, suggesting the presence of a third body in the system.

successfully performed for Kepler-419 b and c (Dawson et al. 2012, 2014). We also note that no transit-duration variations were found.

The orbital astrometric motion of an outer companion could be retrieved from Gaia in the upcoming release of astrometric solutions for ∼1.3 billion stars (Lindegren et al. 2021b). When archival Hipparchos and Gaia observations have been analyzed jointly for previous brighter systems (e.g., Venner et al. 2021), astrometric accelerations have often yielded constraints for outer-stellar massed companions to key exoplanet systems. Additional Gaia observations over the next ∼10 yr will allow us to achieve similar constraints for TOI-4562. Combined with the diffraction-limited adaptive optics observations estimated to

Table 3
Next 10 Transit Opportunities for TOI-4562b

Transit Mid-time (BJD)	Transit Date	Visible from (Partial (P) or Full (F))	TESS Simultaneity
2,460,032.6977	29-Mar-2023	Paranal (P)	Y
2,460,257.8142	9-Nov-2023	Paranal (P)	TBD
2,460,482.9307	21-Jun-2024	MKO (P) and ASTEP (F)	TBD
2,460,708.0473	1-Feb-2025	MKO (F)	TBD
2,460,933.1638	14-Sep-2025	MKO (P) and ASTEP (F)	TBD
2,461,158.2803	27-Apr-2026	SAAO (P) and RUN (P) & ASTEP (F)	TBD
2,461,383.3968	8-Dec-2026	SAAO (P) and RUN (F)	TBD
2,461,608.5134	27-Jul-2027	ASTEP (P)	TBD
2,461,833.6299	3-Mar-2028	SAAO (P) and Paranal (F)	TBD

Note. SAAO: South African Astronomical Observatory, South Africa (latitude = −32.379444, longitude = −339.189306); Paranal: European Southern Observatory at Paranal, Chile (latitude = −24.625, longitude = −70.403333); MKO: Mt. Kent Observatory, Australia (latitude = −27.797861, longitude = 151.855417); RUN: Observatoire astronomique des Makes, Reunion Island (latitude = −21.199359, longitude = 55.409464); ASTEP: Antarctic Search for Transiting ExoPlanets, Dome C, Antarctica (latitude = −75.09978, longitude = 123.332196).

reach ∼35 au (see Section 2.5), these constraints can inform the presence of exterior stellar companions and provide means to distinguish between evolution scenarios.

Another candidate tracer for dynamical history is the angle between the star's rotation axis and the planet's orbital axis, or (sky-projected) obliquity. From $P_\star$, $R_\star$, and $v \sin i$, we estimate the stellar inclination with respect to the line of sight to have a 3σ lower bound of 70° as per Masuda & Winn (2020), consistent with being well aligned. Similarly to other planetary characteristics, the young (<1 Gyr) end of the obliquity distribution is undersampled. Recent measurements resulting from TESS discoveries reveal a remarkable systematic alignment of young systems, including the Jupiter-sized planet HIP 67522 b (Rizzuto et al. 2020; Heitzmann et al. 2021), as well as a number of smaller planets (e.g., AU Mic b and c, Martioli et al. 2020; Palle et al. 2020; Hirano et al. 2020; Plavchan et al. 2020; Addison et al. 2021; DS Tuc Ab, Newton et al. 2019; Montet et al. 2020; Zhou et al. 2020; TOI 942 b and c, Wirth et al. 2021; and TOI 251, Zhou et al. 2021). The estimated amplitude of the Rossiter–McLaughlin effect (Rossiter 1924; McLaughlin 1924) for TOI-4562b is $\Delta V \sim 70$–150 m s^{-1}. Given the ∼4 hr transit duration, combined with a brightness of $V = 12.098$ and a rotational broadening of $v \sin i = 17.5$ km s^{-1}, this is well within the grasp of a 4m class telescope, and such an eccentric system would provide a precious addition to the age-obliquity distribution. It is important to note that the long orbital period remains a major obstacle to transit spectroscopy for ground-based facilities.

In the coming years, we aim to conduct extensive follow-ups of the TOI-4562 system to unravel the full architecture of the system and potentially provide insights into the processes shaping the current gas-giant planet distribution. Such follow-up will include radial velocities, ground- and space-based photometry, astrometry and transit spectroscopy for obliquity measurements, and/or atmospheric characterization.

We respectfully acknowledge the traditional custodians of the lands on which we conducted this research and throughout Australia. We recognize their continued cultural and spiritual connection to the land, waterways, cosmos and community. We pay our deepest respects to all Elders, present and emerging people of the Giabal, Jarowair and Kambuwal nations, upon whose lands the MINERVA-Australis facility at Mount Kent is located. This research has been supported by an Australian Government Research Training Program Scholarship. G.Z. thanks the support of the ARC DECRA program DE210101893. G.Z. and S.Q. thank the support of the TESS Guest Investigator Program G03007. C.H. thanks the support of the ARC DECRA program DE200101840. E.G. gratefully acknowledges support from the David and Claudia Harding Foundation in the form of a Winton Exoplanet Fellowship. This work was supported by an LSSTC Catalyst Fellowship awarded by LSST Corporation to TD with funding from the John Templeton Foundation grant ID # 62192. This research has used data from the CTIO/SMARTS 1.5 m telescope, which is operated as part of the SMARTS Consortium by RECONS This work has made use of data from the European Space Agency (ESA) mission Gaia (https://www.cosmos.esa.int/gaia), processed by the Gaia Data Processing and Analysis Consortium (DPAC, https://www.cosmos.esa.int/web/gaia/dpac/consortium). Funding for the DPAC has been provided by national institutions, in particular the institutions participating in the Gaia Multilateral Agreement. This work makes use of observations from the LCOGT network. Part of the LCOGT telescope time was granted by NOIRLab through the Mid-Scale Innovations Program (MSIP). MSIP is funded by NSF. This research has made use of the NASA Exoplanet Archive, which is operated by the California Institute of Technology, under contract with the National Aeronautics and Space Administration under the Exoplanet Exploration Program. Funding for the TESS mission is provided by NASA's Science Mission directorate. We acknowledge the use of public TESS Alert data from pipelines at the TESS Science Office and at the TESS Science Processing Operations Center. This research has made use of the Exoplanet Follow-up Observation Program website, which is operated by the California Institute of Technology, under contract with the National Aeronautics and Space Administration under the Exoplanet Exploration Program. This paper includes data collected by the TESS mission, which are publicly available from the Mikulski Archive for Space Telescopes (MAST). Resources supporting this work were provided by the NASA High-End Computing (HEC) Program through the NASA Advanced Supercomputing (NAS) Division at Ames Research Center for the production of the SPOC data products. The Center for Exoplanets and Habitable Worlds is supported by the Pennsylvania State University and the Eberly College of Science. R.B. and M.H. acknowledge support from

Table 4
CHIRON Radial Velocities for TOI-4562

BJD	RV (m s^{-1})	BJD	RV (m s^{-1})
2,457,919.279641	5362.7 ± 78.4	2,457,951.584780	5312.4 ± 84.9
2,457,919.975844	5384.0 ± 107.5	2,457,951.882422	5298.0 ± 99.8
2,457,920.077478	5338.8 ± 64.0	2,457,952.183280	5356.5 ± 69.2
2,457,920.770002	5472.3 ± 80.6	2,457,952.483116	5341.9 ± 81.1
2,457,923.866595	5150.9 ± 69.1	2,457,952.785734	5291.7 ± 116.4
2,457,924.163829	5375.4 ± 96.4	2,457,953.181198	5283.6 ± 75.4
2,457,926.463031	5361.0 ± 110.4	2,457,953.478271	5374.3 ± 68.4
2,457,926.769474	5386.8 ± 75.5	2,457,953.779370	5412.8 ± 62.9
2,457,927.459646	5307.2 ± 64.6	2,457,954.078933	5331.6 ± 90.0
2,457,927.755236	5311.9 ± 93.8	2,457,954.477875	5593.4 ± 68.6
2,457,928.059467	5417.3 ± 78.6	2,457,954.770163	5464.1 ± 66.4
2,457,928.466230	5204.1 ± 138.8	2,457,955.179212	5513.8 ± 94.8
2,457,928.761200	5199.1 ± 80.0	2,457,955.280537	5461.7 ± 89.2
2,457,929.259193	5241.1 ± 77.4	2,457,955.375845	5543.3 ± 92.6
2,457,929.558164	5370.1 ± 111.4	2,457,955.482781	5522.4 ± 82.3
2,457,929.953730	5152.4 ± 83.3	2,457,955.578297	5313.6 ± 101.5
2,457,930.253505	5155.4 ± 127.6	2,457,955.677910	5531.5 ± 77.8
2,457,930.457509	5435.7 ± 74.4	2,457,955.978882	5386.7 ± 76.3
2,457,930.752931	5245.4 ± 135.4	2,457,956.078722	5357.4 ± 49.4
2,457,931.049893	5485.1 ± 54.3	2,457,956.174936	5429.0 ± 78.6
2,457,931.459114	5335.7 ± 122.9	2,457,956.268873	5451.4 ± 128.8
2,457,931.852818	5329.3 ± 89.8	2,457,956.477261	5454.5 ± 88.7
2,457,932.354462	5475.9 ± 87.3	2,457,956.567821	5509.4 ± 74.6
2,457,932.753588	4941.1 ± 191.1	2,457,956.671976	5411.0 ± 75.6
2,457,932.950353	5350.4 ± 77.1	2,457,956.776594	5372.3 ± 78.1
2,457,933.157726	5182.6 ± 112.6	2,457,956.872101	5522.2 ± 121.3
2,457,933.548574	5679.6 ± 112.6	2,457,956.968008	5465.6 ± 120.6
2,457,934.251269	5352.0 ± 77.5	2,457,957.070850	5581.7 ± 80.9
2,457,934.548758	5707.1 ± 88.4	2,457,957.173735	5413.1 ± 59.1
2,457,934.949392	5777.3 ± 104.8	2,457,957.273394	5376.5 ± 83.0
2,457,935.148356	5684.9 ± 160.8	2,457,959.269741	5373.7 ± 120.7
2,457,935.644737	5348.6 ± 74.5	2,457,959.369361	5139.8 ± 94.1
2,457,935.744986	5126.8 ± 101.0	2,457,959.565821	5321.7 ± 74.9
2,457,936.045174	5124.1 ± 104.9	2,457,959.662741	5260.0 ± 81.5
2,457,936.146598	5314.9 ± 84.3	2,457,959.765341	5220.0 ± 60.7
2,457,936.345446	5322.3 ± 119.3	2,457,959.861135	5383.7 ± 87.1
2,457,936.438155	5581.4 ± 114.3	2,457,959.969637	5298.7 ± 108.3
2,457,936.545021	5093.0 ± 100.9	2,457,960.060741	5323.5 ± 60.7
2,457,936.646301	5255.5 ± 74.4	2,457,960.162519	5330.1 ± 87.7
2,457,936.744909	5271.4 ± 71.9	2,457,960.265488	5354.1 ± 53.1
2,457,936.846528	5428.8 ± 89.1	·	·
2,457,936.947656	5270.0 ± 69.6	·	·
2,457,937.046070	5415.1 ± 119.0	·	·
2,457,937.145298	5446.5 ± 132.6	·	·

Note. The two left columns cover TOI-4562b's first orbit (late 2020 to mid-2021), and the two right columns cover the second orbit (late 2021 to early 2022).

ANID—Millennium Science Initiative—ICN12_009. N.E. thanks everyone who takes part in the Planet Hunters TESS citizen science project, which contributes to finding new and exciting planetary systems.

Facilities: TESS, Exoplanet Archive, CTIO 1.5 m, LCOGT, Gemini: Zorro, CTIO SOAR, ESO 2.2 m.

Software: ASTROIMAGEJ (Collins et al. 2017), ASTROPY (Astropy Collaboration et al. 2013, 2018), BAFFLES (Stanford-Moore et al. 2020), BATMAN (Kreidberg 2015), CELERITE (Foreman-Mackey et al. 2017), EMCEE (Foreman-Mackey et al. 2013), PYASTRONOMY (Czesla et al. 2019), COMOVE (https://github.com/adamkraus/Comove), PYPHOT (https://mfouesneau.github.io/pyphot/), RADVEL (Fulton et al. 2018), SCIKIT-LEARN (Pedregosa et al. 2011), MINIMINT (https://zenodo.org/record/4900576), NUMPY (Harris et al. 2020), MATPLOTLIB (Hunter 2007), ASTROPY (Astropy Collaboration et al. 2013, 2018), UNRED (https://github.com/pbrus/unredden-stars), PANDAS (pandas development team,T 2020), CORNER (Foreman-Mackey 2016).

ORCID iDs

Alexis Heitzmann https://orcid.org/0000-0002-8091-7526
George Zhou https://orcid.org/0000-0002-4891-3517
Samuel N. Quinn https://orcid.org/0000-0002-8964-8377
Chelsea X. Huang https://orcid.org/0000-0003-0918-7484
Jiayin Dong https://orcid.org/0000-0002-3610-6953

L. G. Bouma https://orcid.org/0000-0002-0514-5538
Rebekah I. Dawson https://orcid.org/0000-0001-9677-1296
Stephen C. Marsden https://orcid.org/0000-0001-5522-8887
Duncan Wright https://orcid.org/0000-0001-7294-5386
Pascal Petit https://orcid.org/0000-0001-7624-9222
Karen A. Collins https://orcid.org/0000-0001-6588-9574
Khalid Barkaoui https://orcid.org/0000-0003-1464-9276
Robert A. Wittenmyer https://orcid.org/0000-0001-9957-9304
Edward Gillen https://orcid.org/0000-0003-2851-3070
Rafael Brahm https://orcid.org/0000-0002-9158-7315
Melissa Hobson https://orcid.org/0000-0002-5945-7975
Coel Hellier https://orcid.org/0000-0002-3439-1439
Carl Ziegler https://orcid.org/0000-0002-0619-7639
César Briceño https://orcid.org/0000-0001-7124-4094
Nicholas Law https://orcid.org/0000-0001-9380-6457
Andrew W. Mann https://orcid.org/0000-0003-3654-1602
Steve B. Howell https://orcid.org/0000-0002-2532-2853
Crystal L. Gnilka https://orcid.org/0000-0003-2519-6161
Colin Littlefield https://orcid.org/0000-0001-7746-5795
David W. Latham https://orcid.org/0000-0001-9911-7388
Jack J. Lissauer https://orcid.org/0000-0001-6513-1659
Elisabeth R. Newton https://orcid.org/0000-0003-4150-841X
Daniel M. Krolikowski https://orcid.org/0000-0001-9626-0613
Ronan Kerr https://orcid.org/0000-0002-6549-9792
Rayna Rampalli https://orcid.org/0000-0001-7337-5936
Stephanie T. Douglas https://orcid.org/0000-0001-7371-2832
Nora L. Eisner https://orcid.org/0000-0002-9138-9028
Nathalie Guedj https://orcid.org/0000-0002-1955-9766
Guoyou Sun https://orcid.org/0000-0003-3162-3350
Tristan Guillot https://orcid.org/0000-0002-7188-8428
George Ricker https://orcid.org/0000-0003-2058-6662
Roland Vanderspek https://orcid.org/0000-0001-6763-6562
Sara Seager https://orcid.org/0000-0002-6892-6948
Jon M. Jenkins https://orcid.org/0000-0002-4715-9460
Eric B. Ting https://orcid.org/0000-0002-8219-9505
Joshua N. Winn https://orcid.org/0000-0002-4265-047X
David R. Ciardi https://orcid.org/0000-0002-5741-3047
Andrew M. Vanderburg https://orcid.org/0000-0001-7246-5438
Christopher J. Burke https://orcid.org/0000-0002-7754-9486
David R. Rodriguez https://orcid.org/0000-0003-1286-5231
Tansu Daylan https://orcid.org/0000-0002-6939-9211

References

Addison, B. C., Horner, J., Wittenmyer, R. A., et al. 2021, AJ, 162, 137
Astropy Collaboration, Price-Whelan, A. M., Sipőcz, B. M., et al. 2018, AJ, 156, 123
Astropy Collaboration, Robitaille, T. P., Tollerud, E. J., et al. 2013, A&A, 558, A33
Baraffe, I., Chabrier, G., & Barman, T. 2008, A&A, 482, 315
Baraffe, I., Chabrier, G., Barman, T. S., Allard, F., & Hauschildt, P. H. 2003, A&A, 402, 701
Barnes, S. A. 2007, ApJ, 669, 1167
Baruteau, C., Crida, A., Paardekooper, S. J., et al. 2014, Protostars and Planets VI, ed. H. Beuther et al. (Tucson, AZ: Univ. Arizona Press), 667
Batygin, K., & Stevenson, D. J. 2010, ApJL, 714, L238
Bianchi, L., Shiao, B., & Thilker, D. 2017, ApJS, 230, 24
Boisse, I., Moutou, C., Vidal-Madjar, A., et al. 2009, A&A, 495, 959
Bouma, L. G., Curtis, J. L., Masuda, K., et al. 2022a, AJ, 163, 121
Bouma, L. G., Hartman, J. D., Brahm, R., et al. 2020, AJ, 160, 239
Bouma, L. G., Kerr, R., Curtis, J. L., et al. 2022b, AJ, 164, 215
Bouvier, J., Barrado, D., Moraux, E., et al. 2018, A&A, 613, A63
Brahm, R., Jordán, A., & Espinoza, N. 2017a, PASP, 129, 034002
Brahm, R., Jordán, A., Hartman, J., & Bakos, G. 2017b, MNRAS, 467, 971
Brown, T. M., Baliber, N., Bianco, F. B., et al. 2013, PASP, 125, 1031
Buchhave, L. A., Latham, D. W., Johansen, A., et al. 2012, Natur, 486, 375
Buder, S., Sharma, S., Kos, J., et al. 2021, MNRAS, 506, 150
Castelli, F., & Kurucz, R. L. 2004, A&A, 419, 725
Chabrier, G., Johansen, A., Janson, M., & Rafikov, R. 2014, Protostars and Planets VI ed. H. Beuther et al., 619
Chatterjee, S., Ford, E. B., Matsumura, S., & Rasio, F. A. 2008, ApJ, 686, 580
Choi, J., Dotter, A., Conroy, C., et al. 2016, ApJ, 823, 102
Claret, A. 2017, A&A, 600, A30
Claret, A., & Bloemen, S. 2011, A&A, 529, A75
Coelho, P. R. T. 2014, MNRAS, 440, 1027
Collins, K. A., Kielkopf, J. F., Stassun, K. G., & Hessman, F. V. 2017, AJ, 153, 77
Cummings, J. D., Deliyannis, C. P., Maderak, R. M., & Steinhauer, A. 2017, AJ, 153, 128
Curtis, J. L., Agueros, M. A., Douglas, S. T., & Meibom, S. 2019, ApJ, 879, 49
Cutri, R. M., Wright, E. L., Conrow, T., et al. 2021, yCatII/328
Czesla, S., Schröter, S., Schneider, C. P., et al. 2019, PyA: Python astronomy-related packages, https://github.com/sczesla/PyAstronomy
Dalba, P. A., Kane, S. R., Dragomir, D., et al. 2022, AJ, 163, 61
David, T. J., Cody, A. M., Hedges, C. L., et al. 2019b, AJ, 158, 79
David, T. J., Petigura, E. A., Luger, R., et al. 2019a, ApJL, 885, L12
Dawson, R. I., & Johnson, J. A. 2018, ARA&A, 56, 175
Dawson, R. I., Johnson, J. A., Fabrycky, D. C., et al. 2014, ApJ, 791, 89
Dawson, R. I., Johnson, J. A., Morton, T. D., et al. 2012, ApJ, 761, 163
Dawson, R. I., Murray-Clay, R. A., & Johnson, J. A. 2015, ApJ, 798, 66
Debras, F., Baruteau, C., & Donati, J.-F. 2021, MNRAS, 500, 1621
Dong, J., Huang, C. X., Zhou, G., et al. 2022, ApJL, 926, L7
Dong, S., Katz, B., & Socrates, A. 2014, ApJL, 781, L5
Douglas, S. T., Agueros, M. A., Covey, K. R., et al. 2016, ApJ, 822, 47
Douglas, S. T., Curtis, J. L., Agueros, M. A., et al. 2019, ApJ, 879, 100
Duffell, P. C., & Chiang, E. 2015, ApJ, 812, 94
Duncan, D. K., Vaughan, A. H., Wilson, O. C., et al. 1991, ApJS, 76, 383
Eastman, J., Gaudi, B. S., & Agol, E. 2013, PASP, 125, 83
Fitzpatrick, E. 1999, PASP, 111, 63
Ford, E. B., & Rasio, F. A. 2006, ApJL, 638, L45
Foreman-Mackey, D. 2016, JOSS, 1, 24
Foreman-Mackey, D., Agol, E., Angus, R., et al. 2017, AJ, 154, 220
Foreman-Mackey, D., Hogg, D. W., Lang, D., & Goodman, J. 2013, PASP, 125, 306
Fortney, J. J., Marley, M. S., & Barnes, J. W. 2007, ApJ, 659, 1661
Fulton, B. J., Petigura, E. A., Blunt, S., & Sinukoff, E. 2018, PASP, 130, 044504
Gagne, J., Mamajek, E. E., Malo, L., et al. 2018, ApJ, 856, 23
Gaia Collaboration, Prusti, T., de Bruijne, J. H. J., et al. 2016, A&A, 595, A1
Gaia Collaboration, Vallenari, A., et al. 2021, A&A, 649, A1
Gillen, E., Briegal, J. T., Hodgkin, S. T., et al. 2020, MNRAS, 492, 1008
Goldreich, P., & Soter, S. 1966, Icar, 5, 375
Guerrero, N. M., Seager, S., Huang, C. X., et al. 2021, ApJS, 254, 39
Guillot, T., Abe, L., Agabi, A., et al. 2015, AN, 336, 638
Guillot, T., & Showman, A. P. 2002, A&A, 385, 156
Hamers, A. S., Antonini, F., Lithwick, Y., Perets, H. B., & Portegies Zwart, S. F. 2017, MNRAS, 464, 688
Harris, C. R., Millman, K. J., van der Walt, S. J., et al. 2020, Natur, 585 357
Heitzmann, A., Zhou, G., Quinn, S. N., et al. 2021, ApJL, 922, L1
Henden, A. A., Templeton, M., Terrell, D., et al. 2016, VizieR Online Data Catalog, yCat, II/336
Hirano, T., Krishnamurthy, V., Gaidos, E., et al. 2020, ApJL, 899, L13
Howell, S. B., Everett, M. E., Sherry, W., Horch, E., & Ciardi, D. R. 2011, AJ, 142, 19
Howell, S. B., & Furlan, E. 2022, FrASS, 9, 871163
Huang, C. X., Vanderburg, A., Pál, A., et al. 2020, RNAAS, 4, 204
Hunter, J. D. 2007, CSE, 9, 90
Jayasinghe, T., Stanek, K. Z., Kochanek, C. S., et al. 2019, MNRAS, 485, 961
Jenkins, J. M. 2002, ApJ, 575, 493

Jenkins, J. M., Tenenbaum, P., Seader, S., et al. 2020, Kepler Science Document KSCI-19081-003, 9
Jenkins, J. M., Radziwill, Nicole M., Bridger, A., et al. 2010, Proc. SPIE, 7740, 77400D
Jenkins, J. M., Twicken, J. D., McCauliff, S., et al. 2016, Proc. SPIE, 9913, 99133E
Kaufer, A., Stahl, O., Tubbesing, S., et al. 1999, Msngr, 95, 8
Kipping, D. M. 2014, MNRAS, 440, 2164
Koposov, S. 2021, segasai/minimint: Minimint v0.3.0, Zenodo, doi:10.5281/zenodo.5610692
Kounkel, M., & Covey, K. 2019, AJ, 158, 122
Kovacs, G., Zucker, S., & Mazeh, T. 2002, A&A, 391, 369
Kozai, Y. 1962, AJ, 67, 591
Kreidberg, L. 2015, PASP, 127, 1161
Lanza, A. F., Rodono, M., & Zappala, R. A. 1993, A&A, 269, 351
Li, J., Tenenbaum, P., Twicken, J. D., et al. 2019, PASP, 131, 024506
Lidov, M. L. 1962, P&SS, 9, 719
Lindegren, L., Bastian, U., Biermann, M., et al. 2021a, A&A, 649, A4
Lindegren, L., Klioner, S. A., Hernández, J., et al. 2021b, A&A, 649, A2
Linder, E. F., Mordasini, C., Molliere, P., et al. 2019, A&A, 623, A85
Lomb, N. R. 1976, Ap&SS, 39, 447
Mamajek, E. E., & Hillenbrand, L. A. 2008, ApJ, 687, 1264
Mandel, K., & Agol, E. 2002, ApJL, 580, L171
Mann, A. W., Johnson, M. C., Vanderburg, A., et al. 2020, AJ, 160, 179
Mann, A. W., Wood, M. L., Schmidt, S. P., et al. 2021, AJ, 163, 156
Martioli, S., Hébrard, G., Moutou, C., et al. 2020, A&A, 641, L1
Masuda, K., & Winn, J. N. 2020, AJ, 159, 81
McCully, C., Volgenau, N. H., Harbeck, D.-R., et al. 2018, Proc. SPIE, 10707
McLaughlin, D. B. 1924, ApJ, 60, 22
Meibom, S., Barnes, S. A., Platais, I., et al. 2015, Natur, 517, 589
Mékarnia, D., Guillot, T., Rivet, J.-P., et al. 2016, MNRAS, 463, 45
Méndez, A., & Rivera-Valentín, E. G. 2017, ApJL, 837, L1
Messina, S., Nardiello, D., Desidera, S., et al. 2022, A&A, 657, L3
Montet, B. T., Feinstein, A. D., Luger, R., et al. 2020, AJ, 159, 112
Morris, B. M. 2020, ApJ, 893, 67
Morris, R. L., Twicken, J. D., Smith, J. C., et al. 2020, Kepler Science Document KSCI-19081-003, 6
Nagasawa, M., Ida, S., & Bessho, T. 2008, ApJ, 678, 498
Nagasawa, M., Lin, D. N. C., & Ida, S. 2003, ApJ, 586, 1374
Naoz, S. 2016, ARA&A, 54, 441
Newton, E. R., Mann, A. W., Tofflemire, B. M., et al. 2019, ApJL, 880, L17
Newton, E. R., Rampalli, R., Kraus, A. L., et al. 2022, AJ, 164, 115
Noyes, R. W., Hartmann, L. W., Baliunas, S. L., Duncan, D. K., & Vaughan, A. H. 1984, ApJ, 279, 763
Oh, S., Price-Whelan, A. M., Hogg, D. W., Morton, T. D., & Spergel, D. N. 2017, AJ, 153, 257
Palle, E., Oshagh, M., Casasayas-Barris, N., et al. 2020, A&A, 643, A25
2020, pandas development team, Tpandas-dev/pandas: Pandas, version: 1.5.3, Zenodo, doi:10.5281/zenodo.3509134
Paredes, L. A., Henry, T. J., Quinn, S. N., et al. 2021, AJ, 162, 176
Paxton, B., Bildsten, L., Dotter, A., et al. 2011, ApJS, 192, 3
Paxton, B., Cantiello, M., Arras, P., et al. 2013, ApJS, 208, 4
Paxton, B., Marchant, P., Schwab, J., et al. 2015, ApJS, 220, 15
Pedregosa, F., Varoquaux, G., Gramfort, A., et al. 2011, JMLR, 12, 2825
Plavchan, P., Barclay, T., Gagné, J., et al. 2020, Natur, 582, 497
Pollacco, D. L., Skillen, I., Cameron, A. C., et al. 2006, PASP, 118, 1407
Rasio, F. A., & Ford, E. B. 1996, Sci, 274, 954
Rauer, H., Catala, C., Aerts, C., et al. 2014, ExA, 38, 249
Rebull, L. M., Stauffer, J. R., Bouvier, J., et al. 2016, AJ, 152, 113
Reinhold, T., Reiners, A., & Basri, G. 2013, A&A, 560, A4
Ricker, G. R., Winn, J. N., Vanderspek, R., et al. 2015, JATIS, 1, 014003
Rizzuto, A. C., Newton, E. R., Mann, A. W., et al. 2020, AJ, 160, 33
Rodet, L., Su, Y., & Lai, D. 2021, ApJ, 913, 104
Rossiter, R. A. 1924, ApJ, 60, 15
Scargle, J. D. 1982, ApJ, 263, 835
Schlafly, E. F., & Finkbeiner, D. P. 2011, ApJ, 737, 103
Sestovic, M., Demory, B.-O., & Queloz, D. 2018, A&A, 616, A76
Shappee, B., Prieto, J., Stanek, K. Z., et al. 2014, AAS Meeting Abstracts, 223, 236
Shara, M. M., Hurley, J. R., & Mardling, R. A. 2016, ApJ, 816, 59
Skrutskie, M. F., Cutri, R. M., Stiening, R., et al. 2006, AJ, 131, 1163
Soderblom, D. R. 2010, ARA&A, 48, 581
Spada, F., & Lanzafame, A. C. 2020, A&A, 636, A76
Stanford-Moore, S. A., Nielsen, E. L., De Rosa, R. J., Macintosh, B., & Czekala, I. 2020, ApJ, 898, 27
Stassun, K. G., Oelkers, R. J., Pepper, J., et al. 2018, AJ, 156, 102
Suárez Mascareño, A., Damasso, M., Lodieu, N., et al. 2022, NatAs, 6, 232
Šubjak, J., Endl, M., Chaturvedi, P., et al. 2022, A&A, 662, 107
Tayar, J., Claytor, Z. R., Huber, D., & van Saders, J. 2022, ApJ, 927, 31
Tofflemire, B. M., Rizzuto, A. C., Newton, E. R., et al. 2021, AJ, 161, 171
Tokovinin, A. 2018, PASP, 130, 035002
Tokovinin, A., Fischer, D. A., Bonati, M., et al. 2013, PASP, 125, 1336
Twicken, J. D., Clarke, B. D., Bryson, S. T., et al. 2010, Proc. SPIE, 7740, 774023
Twicken, J. D., Catanzarite, J. H., Clarke, B. D., et al. 2018, PASP, 130, 064502
Ujjwal, K., Kartha, S. S., Mathew, B., Manoj, P., & Narang, M. 2020, AJ, 159, 166
Vanderburg, A., & Johnson, J. A. 2014, PASP, 126, 948
Venner, A., Vanderburg, A., & Pearce, L. A. 2021, AJ, 162, 12
von Zeipel, H. 1910, AN, 183, 345
Weidenschilling, S. J., & Marzari, F. 1996, Natur, 384, 619
Wirth, C. P., Zhou, G., Quinn, S. N., et al. 2021, ApJL, 917, L34
Wright, E. L., Eisenhardt, P. R. M., Mainzer, A. K., et al. 2010, AJ, 140 1868
Wu, Y., & Lithwick, Y. 2011, ApJ, 735, 109
Zechmeister, M., & Kürster, M. 2009, A&A, 496, 577
Zhou, G., Quinn, S. N., Irwin, J., et al. 2021, AJ, 161, 2
Zhou, G., Winn, J. N., Newton, E. R., et al. 2020, ApJL, 892, L21
Zhou, G., Wirth, C. P., Huang, C. X., et al. 2022, AJ, 163, 289
Ziegler, C., Tokovinin, A., Briceño, C., et al. 2020, AJ, 159, 19
Ziegler, C., Tokovinin, A., Latiolais, M., et al. 2021, AJ, 162, 192